

# PM<sub>2.5</sub> concentrations based on near-surface visibility in the Northern Hemisphere from 1959 to 2022

Hongfei Hao<sup>1</sup>, Kaicun Wang<sup>2</sup>, Guocan Wu<sup>1</sup>, Jianbao Liu<sup>2</sup>, Jing Li<sup>3</sup>

<sup>1</sup>Global Change and Earth System Science, Faculty of Geographical Science, Beijing Normal University, Beijing 100875, China

<sup>2</sup>Institute of Carbon Neutrality, Sino French Institute of Earth System Science, College Urban and Environmental Sciences, Peking University, Beijing 100871, China

<sup>3</sup>Institute of Carbon Neutrality, Sino French Institute of Earth System Science, Department of Atmospheric and Oceanic Sciences, School of Physics, Peking University, Beijing 100871, China

Corresponding Author: *Kaicun Wang* Email: [kcwang@pku.edu.cn](mailto:kcwang@pku.edu.cn)

## Abstract

Long-term PM<sub>2.5</sub> data are essential for the atmospheric environment, human health, and climate change. PM<sub>2.5</sub> measurements are sparsely distributed and of short duration. In this study, daily PM<sub>2.5</sub> concentrations are estimated using a machine learning method from 1959 to 2022 in the Northern Hemisphere based on near-surface atmospheric visibility, which are extracted from the Integrated Surface Database (ISD). Daily continuous monitored PM<sub>2.5</sub> concentration is set as the target, and near-surface atmospheric visibility and other related variables are used as the inputs. The 80% of the samples of each site are the training set, and the 20% are the testing set. The training result shows that the slope of linear regression with a 95% confidence interval (CI) between the estimated PM<sub>2.5</sub> concentration and the monitored PM<sub>2.5</sub> concentration is 0.955 [0.955, 0.955], the coefficient of determination (R<sup>2</sup>) is 0.95, the root mean square error (RMSE) is 7.2 μg/m<sup>3</sup>, and the mean absolute error (MAE) is 3.2 μg/m<sup>3</sup>. The test result shows that the slope within a 95% CI between the predicted PM<sub>2.5</sub> concentration and the monitored PM<sub>2.5</sub> concentration is 0.864 [0.863, 0.865], the R<sup>2</sup> is 0.79, the RMSE is 14.8 μg/m<sup>3</sup>, and the MAE is 7.6 μg/m<sup>3</sup>. Compared with a global PM<sub>2.5</sub> concentration dataset derived from satellite aerosol optical depth product with 1 km resolution, the slopes of linear regression on the daily (monthly) scale are 0.817 (0.854) from 2000 to 2021, 0.758 (0.821) from 2000 to 2010, and 0.867 (0.879) from 2011 to 2022, indicating the accuracy of the model and the consistency of the estimated PM<sub>2.5</sub> concentration on the temporal scale. The interannual trends and spatial patterns of PM<sub>2.5</sub> concentration on the regional scale from 1959 to 2022 are analyzed by Generalized Additive Mixed Model (GAMM), suitable for the situation with an uneven spatial distribution of monitoring sites. The trend is the slope of the Sen-Theil estimator. In Canada, the trend is -0.10 μg/m<sup>3</sup>/decade and the PM<sub>2.5</sub> concentration exhibits an east-high to west-low pattern. In the United States, the trend is -0.40 μg/m<sup>3</sup>/decade, and PM<sub>2.5</sub> concentration decreases significantly after 1992, with a trend of -1.39 μg/m<sup>3</sup>/decade. The high PM<sub>2.5</sub> concentration areas are in the east and west and the low are in the central and northern regions. In Europe, the trend is -1.55 μg/m<sup>3</sup>/decade. High concentration areas are distributed in eastern Europe, and the low areas are in northern and western Europe. In China, the trend is 2.09 μg/m<sup>3</sup>/decade. High concentration areas are distributed in northern China and the low areas are distributed in southern China. The trend is 2.65 μg/m<sup>3</sup>/decade up to 2011 and -22.23 μg/m<sup>3</sup>/decade since 2012. In India, the trend is 0.92 μg/m<sup>3</sup>/decade. The concentration exhibits a north-high to south-low pattern, with high

41 concentration areas distributed in northern India, such as Ganges Plain and Thar Desert and the low  
42 area is in Deccan Plateau. The trend is  $1.41 \mu\text{g}/\text{m}^3/\text{decade}$  up to 2013 and  $-23.36 \mu\text{g}/\text{m}^3/\text{decade}$  since  
43 2014. The variation in regional  $\text{PM}_{2.5}$  concentrations is closely related to the implementation of air  
44 quality laws and regulations. The daily site-scale  $\text{PM}_{2.5}$  concentration dataset from 1959 to 2022 in  
45 the Northern Hemisphere is available at National Tibetan Plateau / Third Pole Environment Data  
46 Center (<https://doi.org/10.11888/Atmos.tpsc.301127>) (Hao et al., 2024).

## 47 **Keywords**

48 Fine particulate matter;  $\text{PM}_{2.5}$ ; Visibility; Machine learning; Dataset.

## 49 **1 Introduction**

50 Fine particulate matter ( $\text{PM}_{2.5}$ ) refers to particulate matter suspended in air with an aerodynamic  
51 diameter of less than 2.5 micrometers.  $\text{PM}_{2.5}$  has various shapes and is composed of complex  
52 components, such as inorganic salts (e.g., sulfate, nitrate, and ammonium), as well as organic carbon  
53 and elemental carbon, metallic elements, and organic compounds (Chen et al., 2020; Fan et al.,  
54 2021).  $\text{PM}_{2.5}$  can be emitted directly into the atmosphere (Viana et al., 2008; Zhang et al., 2019) and  
55 generated through photochemical reactions and transformations (Guo et al., 2014).  $\text{PM}_{2.5}$  exhibits  
56 high concentrations near emission sources, which gradually decreases with distance. Due to the  
57 smaller size and longer life span compared with coarse particulate matter,  $\text{PM}_{2.5}$  can be transported  
58 over long distances by atmospheric movements, leading to wide-ranging impacts. Studies indicate  
59 that regional transport contributes significantly to local  $\text{PM}_{2.5}$  concentration (Wang et al., 2014;  
60 Chen et al., 2020).

61  $\text{PM}_{2.5}$  reduces atmospheric visibility and facilitates the formation of fog and haze conditions (Fan  
62 et al., 2021). Direct and indirect effects of  $\text{PM}_{2.5}$  on solar radiation in the atmosphere (Albrecht,  
63 1989; Ramanathan et al., 2001; Bergstrom et al., 2007; Chen et al., 2022) alter the energy balance  
64 and the number of condensation nuclei, thereby influencing atmospheric circulation and the water  
65 cycle (Wang et al., 2012; Liao et al., 2015; Samset et al., 2019; Li et al., 2022).

66  $\text{PM}_{2.5}$  is also known as respirable particulate matter. Due to its complex composition,  $\text{PM}_{2.5}$  may  
67 carry toxic substances that can significantly impair human health. The World Health Organization  
68 states explicitly that  $\text{PM}_{2.5}$  is more harmful than coarse particles, and long-term exposure to high  
69  $\text{PM}_{2.5}$  concentrations increases the risk of respiratory diseases, cardiovascular diseases, and lung  
70 cancer (Lelieveld et al., 2015), regardless of a country's development status. A Global Burden of  
71 Diseases study reveals that exposure to environmental  $\text{PM}_{2.5}$  causes thousands of deaths and  
72 millions of lung diseases annually (Chafe et al., 2014; Kim et al., 2015; Cohen et al., 2017).

73  $\text{PM}_{2.5}$  is an important parameter for assessing particulate matter pollution and air quality (Wang et  
74 al., 2012).  $\text{PM}_{2.5}$  can lead to soil acidification, water pollution, disruption of plant respiration, and  
75 ecological degradation (Wu and Zhang, 2018; Liu et al., 2019). Due to globalization and economic  
76 integration, preventing and controlling particulate matter pollution is a challenge at city, country  
77 and global scales.

78 Therefore, long-term  $\text{PM}_{2.5}$  concentration data are needed for studies on the environment, human  
79 health, and climate change. At present, ground-based measurements, chemical models, and  
80 estimations of alternatives are the primary sources of  $\text{PM}_{2.5}$  concentration data.

81 Ground-based measurements are the most effective means to measure  $PM_{2.5}$  concentration.  $PM_{2.5}$   
82 monitoring has been ongoing since the 1990s in North America and Europe (Van Donkelaar et al.,  
83 2010), and large-scale  $PM_{2.5}$  monitoring has been implemented in other regions since 2000,  
84 including China in 2013 (Liu et al., 2017). As a result, the records for  $PM_{2.5}$  concentration are short,  
85 with only a few years of data available in many countries. The scarcity of  $PM_{2.5}$  measurements  
86 makes it challenging to provide long-term historical data for research.

87 Many studies have employed statistical methods, machine learning and deep learning methods to  
88 estimate  $PM_{2.5}$  concentrations based on aerosol optical depth. Van Donkelaar et al. (2021) has  
89 utilized satellite aerosol optical depth data, aerosol vertical structure of chemical transport models,  
90 and ground-level measurements to estimate monthly  $PM_{2.5}$  concentrations and their uncertainties  
91 over global land from 1998 to 2019, and there are several related studies (Van Donkelaar et al., 2010;  
92 Boys et al., 2014; Van Donkelaar et al., 2015; Van Donkelaar et al., 2016; Hammer et al., 2020).  
93 Many studies have been conducted at the regional scale, such as in the United States (Beckerman et  
94 al., 2013), China (Wei et al., 2019b; Xue et al., 2019; Wei et al., 2020; He et al., 2021; Wei et al.,  
95 2021), and India (Mandal et al., 2020). Although the  $PM_{2.5}$  concentrations derived from satellite  
96 retrievals have high spatial coverage, there are some limitations that need to be considered. Aerosol  
97 optical depth describes the column property of aerosol, while  $PM_{2.5}$  concentration describes the  
98 near-surface properties of aerosol. Therefore, aerosol vertical structure is crucial in establishing the  
99 relationship between the two. The daily representativeness is also considerable, as  $PM_{2.5}$   
100 concentration is continuously monitored while the daily frequency of satellite observations is low  
101 (1-2 times). Surface types, cloud conditions (Wei et al., 2019a) and resolution (Nagaraja Rao et al.,  
102 1989; Hsu et al., 2017) affect the accuracy of satellite products, thereby increasing uncertainty of  
103 estimation of  $PM_{2.5}$  concentration.

104 Reanalysis datasets provide estimates of long-term particulate matter concentrations. The Modern-  
105 Era Retrospective Analysis for Research and Applications version 2 (MERRA-2) is an excellent  
106 reanalysis dataset from NASA that uses the Goddard Earth Observing System version 5 (GEOS-5),  
107 which provides global  $PM_{2.5}$  data since 1980 (Buchard et al., 2015; Buchard et al., 2016; Buchard  
108 et al., 2017; Gelaro et al., 2017; Sun et al., 2019). There are some emission inventories in the aerosol  
109 model, including: volcanic material; monthly biomass burning from 1980 to 1996; monthly  $SO_2$ ,  
110  $SO_4$ , POM, and BC from 1997 to 2009; annual anthropogenic  $SO_2$  between 100 and 500 m above  
111 the surface from 1980 to 2008; annual anthropogenic  $SO_4$ , BC, and POM concentrations from 1980  
112 to 2006. In assimilation systems, satellite aerosol products from MISR and MODIS Aqua/Terra are  
113 assimilated after 2000. Another reanalysis dataset is the Copernicus Atmosphere Monitoring Service  
114 (CAMS) global reanalysis, which is a global reanalysis dataset of the atmospheric composition  
115 produced by the European Centre for Medium-Range Weather Forecasts (ECMWF) and has  
116 provided  $PM_{2.5}$  data since 2003 (Che et al., 2014; Inness et al., 2019). Although reanalysis provides  
117 long-term  $PM_{2.5}$  data, the uncertainty in emission inventories increases the uncertainty in  $PM_{2.5}$   
118 concentration (Granier et al., 2011). The validation of the reanalysis based on emission inventories  
119 shows that  $PM_{2.5}$  concentration is still overestimated or underestimated in some regions (Buchard  
120 et al., 2017; Ali et al., 2022; Jin et al., 2022). The assimilation of aerosol optical depth products  
121 improves the aerosol column properties (Buchard et al., 2017), thereby improving the estimation of  
122 surface  $PM_{2.5}$  concentration, as it to some extent constrains the vertical structure of aerosols.  
123 However, the lack of high spatiotemporal resolution emission inventories and long-term

124 assimilation data greatly limits the accuracy of surface PM<sub>2.5</sub> concentrations.

125 Another alternative for estimating PM<sub>2.5</sub> concentrations is the near-surface atmospheric horizontal  
126 visibility, which is the maximum distance at which observers with normal visual acuity can discern  
127 target contours under current weather conditions. In addition to manual observations, automated  
128 visibility measurement has been implemented early, typically relying on the aerosol scattering  
129 principle (Wang et al., 2009; Zhang et al., 2020). Both visibility and PM<sub>2.5</sub> concentration are  
130 measurements of near-surface aerosols. They describe atmospheric horizontal transparency and are  
131 used to describe atmospheric pollution. Long-term visibility records have been used to quantify  
132 long-term aerosol properties (Molnár et al., 2008; Wang et al., 2009; Zhang et al., 2017; Zhang et  
133 al., 2020). Visibility observation stations are densely distributed across the world. Compared to  
134 satellite retrievals, visibility observations have longer historical records dating back to the early 20th  
135 century (Noaa et al., 1998; Boers et al., 2015), are not affected by cloud interference and provide  
136 continuous measurements.

137 Visibility has been used as a proxy for PM<sub>2.5</sub> concentration (Huang et al., 2009) and to estimate  
138 PM<sub>2.5</sub> concentration (Liu et al., 2017; Li et al., 2020; Singh et al., 2020). Singh et al. (2020) has  
139 analyzed the air quality in East Africa from 1974 to 2018 using visibility data. Liu et al. (2017) has  
140 developed a statistical model and utilized ground-level visibility data to estimate long-term PM<sub>2.5</sub>  
141 concentrations in China from 1957 to 1964 and 1973 to 2014. Gui et al. (2020) has proposed a  
142 method to establish a virtual ground observation network for PM<sub>2.5</sub> concentration in China using  
143 extreme gradient boosting modeling in 2018. Zeng et al. (2021) has used LightGBM to establish a  
144 virtual network for hourly PM<sub>2.5</sub> concentrations in China in 2017. Zhong et al. (2021; 2022) has  
145 used LightGBM to predict 6-hour PM<sub>2.5</sub> concentrations based on visibility, temperature, and relative  
146 humidity in China from 1960 to 2020. Meng et al. (2018) has utilized a random forest model to  
147 estimate the daily PM<sub>2.5</sub> components in the United States from 2005 to 2015. These studies have  
148 provided various methods for estimating PM<sub>2.5</sub> using visibility data. However, some have focused  
149 on only methodological innovations without providing long-term trends in PM<sub>2.5</sub> concentration.  
150 Other studies offer long-term trends, but the primary focus is at urban or national scale. There are  
151 few studies on long-term and high-temporal-resolution PM<sub>2.5</sub> concentration at the global scale or  
152 across different countries.

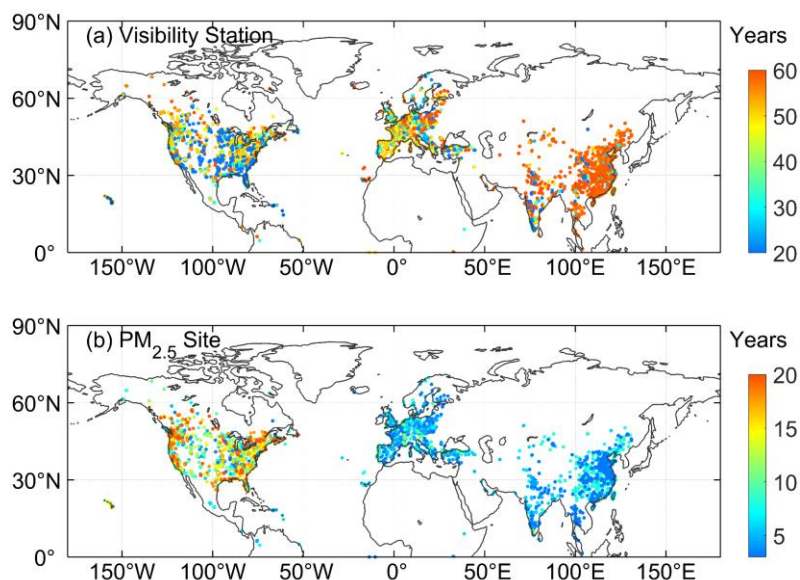
153 This study uses a convenient, accurate, and easily understandable machine learning approach to  
154 estimate daily PM<sub>2.5</sub> concentrations based on visibility at 5023 land-based sites from 1959 to 2022.  
155 First, we build a machine learning model and then analyze the importance of the variables. Second,  
156 we evaluate the model's performance and predictive ability. Third, we discuss the errors and  
157 limitations of the dataset. Fourth, we compare the estimated PM<sub>2.5</sub> concentration with the other  
158 dataset. Finally, we analyze the long-term trends and spatial patterns of PM<sub>2.5</sub> concentration in  
159 different regions. We hope the PM<sub>2.5</sub> dataset will provide support for the atmospheric environment,  
160 human health, and climate change studies.

## 161 **2 Data and methods**

### 162 **2.1 Study Area**

163 The study area is the Northern Hemisphere. Figure 1 shows the distributions of visibility stations (a)  
164 and the PM<sub>2.5</sub> monitoring sites (b). Table 1 lists information of stations such as the number and time

165 span in each region. The number of visibility stations and PM<sub>2.5</sub> monitoring sites is 5023. Due to its  
 166 relevance to national or regional development, the record length and distribution of PM<sub>2.5</sub>  
 167 observation are uneven. In this study, the site-scale PM<sub>2.5</sub> observations are met at least three years.  
 168 These sites are densely populated in North America, East and South Asia, and Europe, and are very  
 169 sparse in regions such as Africa and South America, and West Asia.



170

171 **Figure 1.** Study area and distributions of visibility stations (a) and PM<sub>2.5</sub> monitoring sites (b). The  
 172 color of marker (circle) represents the year number of visibility observations and PM<sub>2.5</sub>  
 173 concentration observations.

174 **Table 1.** Data summary.

	Region	Sites Number	Time Span	Temporal/Spatial Resolution	Data Source
Visibility	Global land	5023	1959-2022	Hourly/-	<a href="https://www.weather.gov/asos">https://www.weather.gov/asos</a>
	the United States	1111	1998-2022	Hourly/-	<a href="https://www.epa.gov/aqs">https://www.epa.gov/aqs</a>
	Canada	311	1995-2022	Hourly/-	<a href="https://www.canada.ca">https://www.canada.ca</a>
PM <sub>2.5</sub> observations	Europe	1073	1998-2022	Hourly/-	<a href="https://european-union.europa.eu">https://european-union.europa.eu</a> ; <a href="https://www.eea.europa.eu">https://www.eea.europa.eu</a>
	China	1887	2014-2022	Hourly/-	<a href="https://www.cnemc.cn">https://www.cnemc.cn</a>
	India	270	2010-2022	Hourly/-	<a href="https://app.cpcbcr.com">https://app.cpcbcr.com</a>
	Other regions	371	2016-2022	Hourly/-	<a href="https://openaq.org">https://openaq.org</a>
LGHAP	Land (-58~62°N)	--	2000-2021	Daily/1km	<a href="https://zenodo.org/communities/ecnu_lghap">https://zenodo.org/communities/ecnu_lghap</a>

## 175 2.2 PM<sub>2.5</sub> Data

### 176 2.2.1 PM<sub>2.5</sub> Data in the United States

177 The hourly PM<sub>2.5</sub> concentration data for the United States from 1998 to 2022 are sourced from the  
 178 Air Data System (AQS), which are available at <https://www.epa.gov/aqs>. The AQS provides PM<sub>2.5</sub>  
 179 mass monitoring and routine chemical speciation data and contains other ambient air pollution data  
 180 collected by the Environmental Protection Agency (EPA), state, local, and tribal air pollution control  
 181 agencies from thousands of monitors, comprising the Federal Reference Method (FRM) and Federal

182 Equivalent Method (FEM). The primary purpose of both methods is to assess compliance with the  
183 PM<sub>2.5</sub> National Ambient Air Quality Standards (NAAQS). FRMs include in-stack particulate  
184 filtration, and FEMs include beta-attenuation monitoring, very sharp cut cyclones, and tapered  
185 element oscillating microbalances (TOEMs). The measurement precision is  $\pm (1\sim 2) \mu\text{g}/\text{m}^3$  (hour)  
186 (Hall and Gilliam, 2016). The TEOM and beta-attenuation are automatic and near real-time  
187 monitoring methods. The TEOM, which is based on gravity, measures the mass of particles collected  
188 on filters by monitoring the frequency changes in tapered elements. The beta-attenuation method  
189 uses beta-ray attenuation and particle mass to measure the PM<sub>2.5</sub> concentration. In this study, we use  
190 two PM<sub>2.5</sub> measurement methods, FRM/FEM (88101) and non-FRM/FEM (88502). The 88502  
191 monitors are “FRM-like” but are not used for regulatory purposes. Both the 88101 and 88502  
192 monitors are used for reporting daily Air Quality Index values.

### 193 **2.2.2 PM<sub>2.5</sub> Data in Canada**

194 The hourly PM<sub>2.5</sub> concentration data for Canada from 1995 to 2022 are sourced from the National  
195 Air Pollution Surveillance (NAPS) program, which are available at <https://www.canada.ca>. The  
196 NAPS program is a collaborative effort between the Environment and Climate Change Canada and  
197 provincial, territorial, and regional governments and is the primary source of environmental air  
198 quality data. Since 1984, PM<sub>2.5</sub> concentrations have been measured in Canada using a dichotomous  
199 sampler. Continuous or real-time particle monitoring began in the NAPS network in 1995 using  
200 TEOM and beta-attenuation monitoring (Demerjian, 2000). The samples are supplemented by EPA  
201 FRM samples obtained after 2009 (Dabek-Zlotorzynska et al., 2011).

### 202 **2.2.3 PM<sub>2.5</sub> Data in Europe**

203 The hourly PM<sub>2.5</sub> concentration data for Europe from 1998 to 2012 are obtained from the AirBase  
204 database, which is available at <https://european-union.europa.eu>. The hourly PM<sub>2.5</sub> concentration  
205 data (E1a) from 2013 to 2022 are obtained from the AirQuality database, which is available at  
206 <https://www.eea.europa.eu>. AirBase is maintained by the European Environment Agency (EEA)  
207 through its European Topic Center on Air Pollution and Climate Change Mitigation. Airbase  
208 contains air quality monitoring data and information submitted by participating countries  
209 throughout Europe. After the Air Quality Directive 2008/50/EC was enforced, the PM<sub>2.5</sub>  
210 concentration data began to be stored in AirQuality database. The main monitoring methods for  
211 PM<sub>2.5</sub> concentration include TEOM and beta attenuation (Green and Fuller, 2006; Chow et al., 2008).  
212 The sites are distributed across rural, rural-near city, rural-regional, rural-remote, suburban, and  
213 urban areas.

### 214 **2.2.4 PM<sub>2.5</sub> Data in China**

215 The hourly PM<sub>2.5</sub> concentration data for China from 2014 to 2022 are obtained from the China  
216 National Environmental Monitoring Center, which are available at <https://www.cnemc.cn>. The  
217 continuous monitoring of PM<sub>2.5</sub> nationwide began in 2013 and PM<sub>2.5</sub> concentration data are  
218 available to the public. (Su et al., 2022), and there are about 2000 air quality observation sites in  
219 2022. PM<sub>2.5</sub> concentrations are measured using the TEOM and beta-attenuation method (Zhao et al.,  
220 2016b; Miao and Liu, 2019). According to the China Environmental Protection Standards,  
221 instrument maintenance, data transmission, data assurance and quality control ensure the reliability  
222 of PM<sub>2.5</sub> concentration measurements. The uncertainty in the PM<sub>2.5</sub> concentration is  $< 5 \mu\text{g}/\text{m}^3$  (Pui

223 et al., 2014).

### 224 **2.2.5 PM<sub>2.5</sub> Data in India**

225 The hourly PM<sub>2.5</sub> concentration data for India from 2010 to 2022 are obtained from the Central  
226 Pollution Control Board (CPCB), which are available at <https://app.cpcbcecr.com>. The Air  
227 (Prevention and Control of Pollution) Act of 1981 is enacted by the Central Pollution Control Board  
228 (CPCB) of the Ministry of Environment, Forest and Climate Change (MoEFCC). The National Air  
229 Quality Monitoring Programme (NQAMP) is a key air quality monitoring programme employed by  
230 the Government of India, which is managed by the CPCB in coordination with the State Pollution  
231 Control Boards (SPCBs) and UT Pollution Control Committees (PCCs). A standard of 60 µg/m<sup>3</sup>  
232 PM<sub>2.5</sub> concentration over 24 hours is added in 2009. The methods used by the Indian National  
233 Ambient Air Quality Standards (NAAQS) for PM<sub>2.5</sub> concentration and related component  
234 measurements include the FRM and FEM (Pant et al., 2019). The measurement precision is ± (1-2)  
235 µg/m<sup>3</sup> (hour).

### 236 **2.2.6 PM<sub>2.5</sub> data in other regions**

237 The hourly PM<sub>2.5</sub> concentration data of other regions from 2016 to 2022 are from openAQ  
238 (<https://openaq.org>), which is a nonprofit organization providing air quality data. These air quality  
239 data are collected from environmental protection departments and other departments over the world  
240 without any processing, therefore they have good accuracy. The PM<sub>2.5</sub> concentrations almost are  
241 measured by the TEOM and beta-attenuation method, and have been used for scientific research  
242 (Jin et al., 2022; Tan et al., 2022).

### 243 **2.3 Visibility and Meteorological Data**

244 The hourly visibility and meteorological data are from the Integrated Surface Database (ISD) (Smith  
245 et al., 2011), which is a global database consisted of hourly and synoptic surface observations and  
246 archived at the NOAA's National Centers for Environmental Information (NCEI), available at  
247 <https://www.ncei.noaa.gov/products/land-based-station/integrated-surface-database>. The ISD  
248 database integrates data from more than 100 original data sources and incorporates data from over  
249 35000 stations around the world and includes observations data dating back to 1901. The strict  
250 quality control algorithms are used to ensure data quality by checking data format, extreme values  
251 and limits, consistency between parameters, and continuity between observations. Detailed  
252 information about the quality control are in [http://www.ncei.noaa.gov/pub/data/inventories/ish-  
253 gc.pdf](http://www.ncei.noaa.gov/pub/data/inventories/ish-gc.pdf). The best spatial coverage of stations is evident in North America, Europe, Australia, and  
254 parts of Asia, and the coverage in the Northern Hemisphere is better than the Southern Hemisphere.

255 Visibility and meteorological records are filtered by the geophysical report type code. The codes of  
256 FM-12 and FM-15 are selected. FM-12 code represents the report is from Surface Synoptic  
257 Observations (SYNOP) report, which is a coding system developed by the World Meteorological  
258 Organization (WMO) for reporting observation data from ground meteorological stations. FM-15  
259 code represents the report is from Meteorological Terminal Aviation Routine Weather Report  
260 (METAR), providing weather information at the airport and its surrounding areas. The format and  
261 content of the METAR report are consistent globally and comply with WMO's international  
262 meteorological observation and reporting standards. The frequency of SYNOP report is generally  
263 every three or six hours, and the frequency of METAR report is usually once per hour.

264 In this study, visibility is an essential variable for PM<sub>2.5</sub> concentration. The reciprocal of visibility  
265 is directly proportional to the aerosol extinction coefficient, which is closely related to the PM<sub>2.5</sub>  
266 concentration (Wang et al., 2009; Wang et al., 2012). Considering that temperature, wind speed,  
267 humidity, and precipitation are factors that impact particle dispersion, particle growth, and  
268 secondary generation (Zhang et al., 2020), temperature, dew point temperature, wind speed, and  
269 precipitation are selected.

## 270 **2.4 Data Preprocessing**

271 When processing the visibility and meteorological variables, we use some screening conditions from  
272 previous studies (Husar et al., 2000; Wang et al., 2009; Li et al., 2016; Zhong et al., 2021). We  
273 remove the records with missing visibility, temperature, dew point temperature, wind speed and  
274 hourly precipitation greater than 0.1 mm. Relative humidity is calculated using the Goff-Gratch  
275 formula (Goff, 1957). When relative humidity is greater than 90%, the record is removed to reduce  
276 the influence of fog, even precipitation. In high latitude regions, the low visibility records caused  
277 by ice fog and snow are removed, when the temperature is less than -29 °C and the wind speed is  
278 greater than 16 km/h. Since PM<sub>2.5</sub> exhibits hygroscopic growth, dry visibility is calculated, when  
279 relative humidity is between 30% and 90% (Yang et al., 2021).

$$280 \quad \mathbf{VISD} = \mathbf{VIS}/(\mathbf{0.26} + \mathbf{0.4285} * \mathbf{log}(100 - \mathbf{RH})) \quad \mathbf{(1)}$$

281 where VIS is the visibility, RH is the relative humidity, and VISD is the dry visibility.

282 For a single visibility site, there should be at least 5 non-repetitive visibility values and at least three  
283 valid records per day. The upper limit of visibility is set to the 99% percentile of visibility (Li et al.,  
284 2016). The harmonic mean is used to calculate the daily VIS and VISD because it can better capture  
285 rapid weather changes and enhance daily representativeness (Noaa et al., 1998). The arithmetic  
286 mean is used for other variables.

287 The maximum hourly PM<sub>2.5</sub> concentration is set to 1000 µg/m<sup>3</sup>. The daily PM<sub>2.5</sub> concentration needs  
288 at least 3 hourly records. We select the PM<sub>2.5</sub> monitoring sites with a condition of at least 3-year  
289 continuous monitoring. The distribution of PM<sub>2.5</sub> sites is shown in Figure 1, and the details are  
290 shown in Table 1.

291 The spatial matching between PM<sub>2.5</sub> site and visibility station adopts the nearest principle, and the  
292 upper limit of distance is set to 100 km. Through experiments that the upper limit of distance has  
293 little effect on model training and prediction, but when the upper limit is small, the number of site  
294 pairs significantly decreases, especially in Asia. Matched visibility stations are not be used again.  
295 To match more PM<sub>2.5</sub> monitoring sites, we construct a 'virtual' visibility station, whose variables are  
296 established by the average of variables of the two nearest visibility stations.

297 We merge daily PM<sub>2.5</sub> concentration and visibility and other meteorological variables. We have  
298 adopted two matching methods: (1) merge at the hourly scale first and then calculate the daily mean  
299 (2) and calculate the daily mean first and then match. The results of two methods have no impact  
300 on the training of the model, but there are differences in the predicted results. Since SNOPY's  
301 visibility is not continuously observed hourly, we select the second method to merge PM<sub>2.5</sub>  
302 concentration and visibility data on the daily scale to improve the daily representativeness of  
303 estimated PM<sub>2.5</sub> concentration.



## 304 **2.5 PM<sub>2.5</sub> Data for Comparison**

305 The long-term gap-free high-resolution air pollutants (LGHAP) dataset provides daily PM<sub>2.5</sub>  
306 concentrations from 2000 to 2021 over global land, with a 1 km grid resolution, which is available  
307 at [https://zenodo.org/communities/ecnu\\_lghap](https://zenodo.org/communities/ecnu_lghap). The PM<sub>2.5</sub> concentration is estimated using aerosol  
308 optical depth and other factors such as geographic location, land cover type, climate zone, and  
309 population density, based on a deep-learning approach, termed the scene-aware ensemble learning  
310 graph attention network. The correlation coefficient with ground-based measurements is 0.95 and  
311 the RMSE is 5.7  $\mu\text{g}/\text{m}^3$  (Bai et al., 2024). This dataset provides global PM<sub>2.5</sub> concentration with a  
312 high spatiotemporal resolution.

313 For most regions in the Northern Hemisphere, except for North America and Europe, the duration  
314 of continuous monitoring PM<sub>2.5</sub> concentration data is relatively short, making it difficult to evaluate  
315 historical PM<sub>2.5</sub> concentration. For example, PM<sub>2.5</sub> monitoring network in China was implemented  
316 from the end of 2012, resulting in the inability to verify the PM<sub>2.5</sub> concentrations before 2012.  
317 Therefore, we compare our data with the LGHAP PM<sub>2.5</sub> concentration to evaluate the predictive  
318 ability of the model and the consistency of our data on the temporal scale.

## 319 **2.6 Decision Tree Regression**

320 We employ decision tree regression (Teixeira, 2004) to estimate daily PM<sub>2.5</sub> concentrations. The key  
321 to decision tree regression is to find the optimal split variable and optimal split point. The optimal  
322 split point of the predictor is determined by the minimum mean squared error, which determines the  
323 optimal tree structure. Decision tree regression is a commonly used nonlinear machine learning  
324 method that partitions the feature space based on the mapping between feature attributes and  
325 response values, with each leaf node representing a specific output for each feature space region.  
326 It's ability to handle complex relationships with relatively few model parameters is advantageous,  
327 minimizing the risk of overfitting and enabling the prediction of continuous and categorical  
328 predictive variables.

329 The sample data includes predictor and response. The predictor is composed of 9 variables: the  
330 reciprocal of dry visibility (Vis\_Dry\_In), the reciprocal of visibility (Vis\_In), temperature (Temp),  
331 dew point temperature (Td), temperature-dew point difference (Temp-Td), relative humidity (RH),  
332 wind speed (WS), wind numerical time (DateTime) and daily record number (DailyObsNum). Both  
333 visibility and meteorological variables are daily means. The response variable is the daily monitored  
334 PM<sub>2.5</sub> concentration.

335 For each site, we sort the sample data by time, with the first 80% being the training set and the last  
336 20% being the test set. Due to the inconsistent sample length among different sites, this approach is  
337 friendly for sites with small sample sizes (such as only 3-year observations). We use 10-fold cross-  
338 validation method (Browne, 2000) to train the model. The test set is used to evaluate the predictive  
339 ability of the model.

## 340 **2.7 Evaluation Metrics**

### 341 **2.7.1 Statistical Metrics**

342 We use the root mean squared error (RMSE), mean absolute error (MAE), and correlation  
343 coefficient ( $\rho$ ) as evaluation metrics to evaluate the model's performance and predictive ability. The

344 formulas are given as follows:

$$345 \quad \mathbf{MSE} = \sqrt{\frac{1}{n} \sum_{i=1}^n (y_i - \hat{y}_i)^2} \quad (2)$$

$$346 \quad \mathbf{MAE} = \frac{1}{n} \sum_{i=1}^n |y_i - \hat{y}_i| \quad (3)$$

$$347 \quad \rho = \frac{\sum_{i=1}^n (y_i - \bar{y})(\hat{y}_i - \bar{\hat{y}})}{\text{sqrt}(\sum_{i=1}^n (y_i - \bar{y})^2 \sum_{i=1}^n (\hat{y}_i - \bar{\hat{y}})^2)} \quad (4)$$

348 where  $y_i$  and  $\bar{y}$  are the predicted value and the average of the predicted values.  $\hat{y}_i$  and  $\bar{\hat{y}}$  are  
 349 the target and the average of the target.  $i = 1, 2, \dots, n$ .  $n$  is the length of sample.

### 350 2.7.2 Partial Dependence

351 The importance of predictor variables is assessed via partial dependence. Partial dependence  
 352 represents the relationship between the individual predictive variable and the predicted response  
 353 (Friedman, 2001). By marginalizing the other variables, the expected response of the predicted  
 354 variable is calculated. All the partial dependences of the predicted response on the subset of  
 355 predicted variables are calculated. The calculation process of the partial dependency method is  
 356 described as follows:

357 The dataset of the predictor is  $X$ ,  $X = [X^1, X^2, \dots, X^n]$ , and  $n$  represents the number of predictive  
 358 factors. The complement of subset  $X^s$  is  $X^c$ , where  $X^s$  is a single variable in  $X$  and  $X^c$  is all  
 359 other variables in  $X$ . The predicted response  $f(x)$  depends on all variables in  $X$ , and it is expressed  
 360 as follows:

$$361 \quad \mathbf{f}(x) = \mathbf{f}(X^s, X^c) \quad (5)$$

362 The partial dependence of the predicted response to  $X^s$  is expressed as follows:

$$363 \quad \mathbf{f}^s(X^s) = \int \mathbf{f}(X^s, X^c) \mathbf{pC}(X^c) dX^c \quad (6)$$

364 where  $\mathbf{pC}(X^c)$  is the marginal probability of  $X^c$ , that is,  $\mathbf{pC}(X^c) \approx \int \mathbf{f}(X^s, X^c) dX^s$ . Assuming  
 365 that the likelihood for each observation is equal, the dependence between  $X^s$  and  $X^c$  and the  
 366 interactions of  $X^s$  and  $X^c$  in response are not strong. The partial dependence is shown below:

$$367 \quad \mathbf{f}^s(X^s) \approx \frac{1}{N} \sum_{i=1}^N \mathbf{f}(X^s, X_i^c) \quad (7)$$

368 where  $N$  is the number of observations and  $i$  represents the  $i$ th observation.

### 369 2.7.3 Generalized Additive Mixed Model

370 Generalized Additive Mixed Model (GAMM) originates from two independent yet complementary  
 371 statistical methods: Generalized Additive Model (GAM) and Mixed Effects Models. GAM is  
 372 introduced by Trevor Hastie and Robert Tibshirani in the 1980s (Hastie and Tibshirani, 1987). GAM  
 373 employs smooth functions (such as splines) to replace linear terms in traditional regression,  
 374 capturing nonlinear relationships between response and explanatory variables. The primary aim of  
 375 GAM is to enhance model flexibility, allowing the data to determine the form of the nonlinear  
 376 relationships rather than pre-specifying them. Mixed Effects Model includes both fixed and random

377 effects, enabling the analysis of hierarchical and correlated data (Verbeke and Lesaffre, 1996). Fixed  
 378 effects apply to the entire sample, whereas random effects account for variations within individuals  
 379 or groups, explaining data correlation and variability. GAMM represents the evolution of statistical  
 380 models from linear to nonlinear, from simple to complex, and from single effects to mixed effects.  
 381 GAMM has been widely applied in various fields such as ecology and climate, air pollution  
 382 becoming essential tools for studying complex nonlinear relationships and hierarchical data (Park  
 383 et al., 2013; Polansky and Robbins, 2013; Chang et al., 2017; Ravindra et al., 2019).

384 The relationship between PM<sub>2.5</sub> concentrations and time (e.g., months, seasons) is typically  
 385 nonlinear and exhibits seasonal variation. GAMM model uses smooth functions (such as splines) to  
 386 capture the nonlinear variations and model the periodic features with cyclical smooth functions.  
 387 Interannual variations in PM<sub>2.5</sub> concentrations can also be captured using smooth functions. Due to  
 388 the inherent autocorrelation in time series, GAMM model effectively handles the autocorrelation by  
 389 incorporating time-related smooth functions or random effects, thereby enhancing the model  
 390 accuracy. PM<sub>2.5</sub> concentrations from neighboring locations often exhibit spatial correlation. GAMM  
 391 model can address this spatial correlation by introducing spatially correlated smooth functions or  
 392 random effects. Therefore, it is also suitable for spatial variations, especially when the spatial  
 393 distribution of sites observations is uneven.

394 Based on the GAMM, the PM<sub>2.5</sub> concentration  $y(i, t)$  at site  $i$  and time  $t$  can be expressed as:

$$395 \mathbf{y}(i, t) = \mathbf{x}\boldsymbol{\beta} + \mathbf{f}(\cdot) + \mathbf{b}(i, t) + \boldsymbol{\varepsilon}(i, t) \quad (8)$$

396 The following is an explanation of the expression and parameter settings.

397 *Linear terms*  $\mathbf{x}\boldsymbol{\beta}$ :  $\mathbf{x}$  is the vector of explanatory variables, including site elevation and the overall  
 398 mean PM<sub>2.5</sub> concentration.  $\boldsymbol{\beta}$  is a coefficient vector.

399 *Smooth terms*  $\mathbf{f}(\cdot)$  can be decomposed into three individual smooth terms: seasonal smooth term,  
 400 interannual smooth term, and spatial smooth term, as shown in equation (9).

$$401 \mathbf{f}(\cdot) = \mathbf{f}(\mathbf{month}) + \mathbf{f}(\mathbf{year}) + \mathbf{f}(\mathbf{spatial}) \quad (9)$$

402 They are composed of linear combinations using spline basis functions. For seasonal smooth term,  
 403 it is a function of the month, smooth function is the penalized regression cyclic cubic splines  
 404 (assumed with periodic nature) (Wood et al., 2016) and the knot number is 12. For interannual  
 405 smooth term, it is a function of the year, smooth function is the penalized regression cubic splines  
 406 (Wood et al., 2016) and the knot number is 64. For spatial smooth term, it is a function for longitude  
 407 and latitude, smooth function is the gaussian process penalized regression splines (Kammann and  
 408 Wand, 2003) and the knot number is 80. In this study, they are used to describe the regional long-  
 409 term PM<sub>2.5</sub> concentration annual cycle, interannual trends and spatial distribution, respectively.

410 Station-specific effects term  $\mathbf{b}(i, t)$  is a random effect term to describe the differences between  
 411 observation sites, based on the assumption that observations are independent.

412 The residual noise term  $\boldsymbol{\varepsilon}(i, t)$  1-order autoregressive term.

413 More explanations about GAMM model are detailed in the package mgcv of R. Some studies also  
 414 provide an introduction and selection of parameters (Polansky and Robbins, 2013; Chang et al.,  
 415 2017; Ravindra et al., 2019).

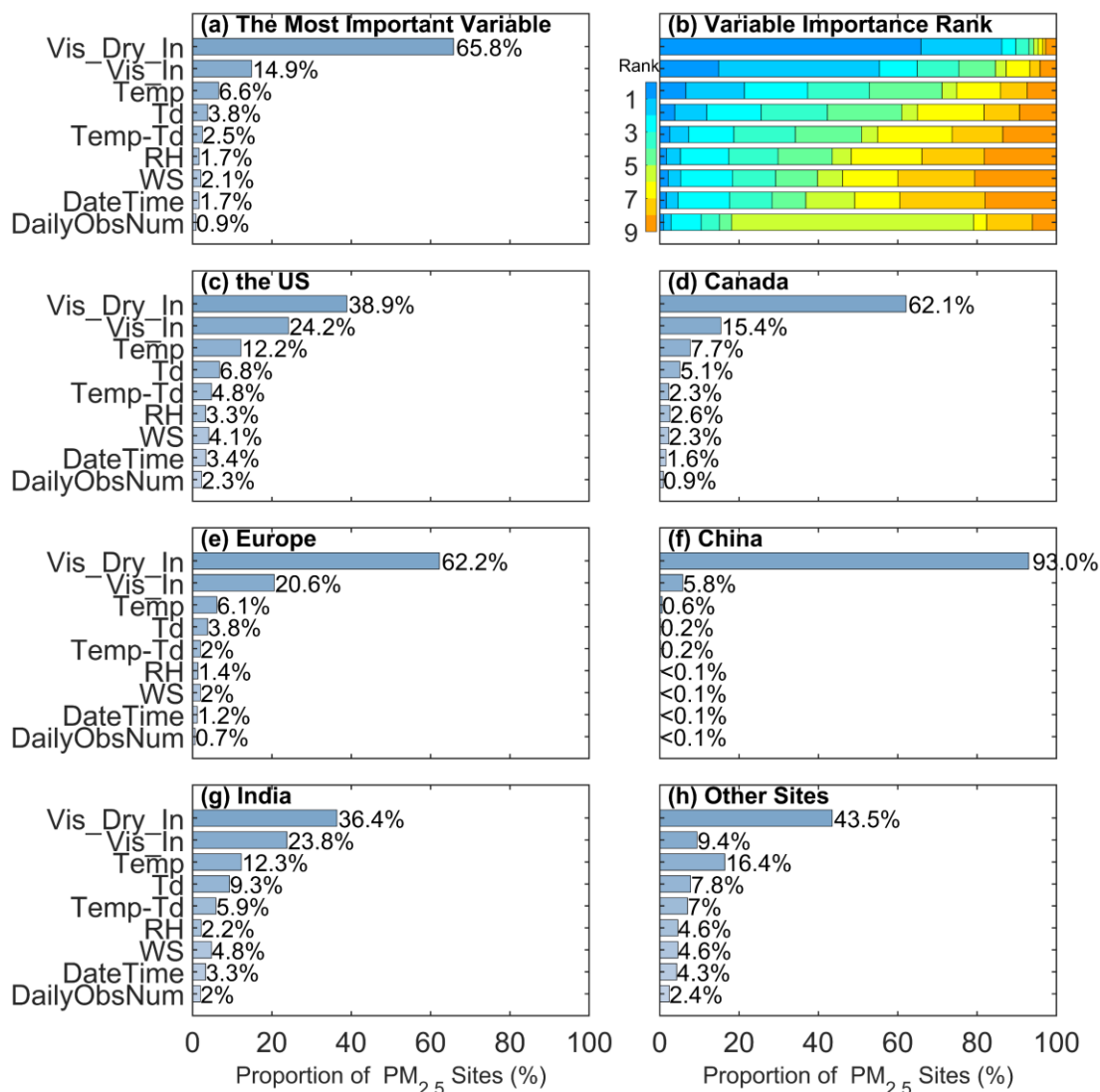
## 416 **3. Results and Discussion**

### 417 **3.1 Evaluation of Variable Importance**

418 We evaluate the contribution of each variable to the response by partial dependence. The variable  
419 with the highest partial dependence value is the most important variable in the model. Figure 2 (a)  
420 shows the proportion of the most important variables for all sites and Figure 2 (b) shows the ranking  
421 of the importance of all variables. Reciprocal of dry visibility is the most important variable at 65.8%  
422 of sites, and Reciprocal of visibility is the second most important variable at 14.9% of sites. The  
423 contribution of meteorological variables ranges from 2.1% to 6.6%. The time variable contributes  
424 1.7%. The lowest contribution is daily number of visibility record at only 0.9%, because it is only a  
425 variable that describes the daily representativeness of visibility. It also indicates that daily visibility  
426 has high daily representativeness (under the conditions of at least three hourly records)

427 The  $PM_{2.5}$  concentration level varies spatially, which are related to regional geographical  
428 environment, climate, and air quality laws and regulations. Therefore, we analyze the importance  
429 of variables in different regions, as shown in Figure 2 (c-h). The two most important variables are  
430 still reciprocal of dry visibility and reciprocal of visibility, with a proportion of 73.1% in the United  
431 States, 77.5% in Canada, 80.8% in Europe, 98.8% in China, and 60.2% in India. It indicates that  
432  $PM_{2.5}$  concentration is the most significantly correlated with visibility in China. The contribution of  
433 meteorological variables is significantly higher in the United States and India than in other regions.  
434 It indicates that meteorological conditions have a significant contribution to  $PM_{2.5}$  concentration in  
435 these regions, which may be related to the formation mechanism and transport of particulate matter.

436 The above results indicate a strong correlation between the  $PM_{2.5}$  concentration and visibility, as  
437 visibility can be considered an indicator of air quality without fog or precipitation. Meteorological  
438 factors play secondary roles, which influence the formation, dispersion and deposition of  $PM_{2.5}$  (Gui  
439 et al., 2020; Zhong et al., 2022). Although the number of daily records and time have the most  
440 negligible impacts on the  $PM_{2.5}$  concentration in the model, they have significant impacts on the  
441 cyclical changes and daily representativeness of  $PM_{2.5}$  concentration (Wang et al., 2012; Zhang et  
442 al., 2020).

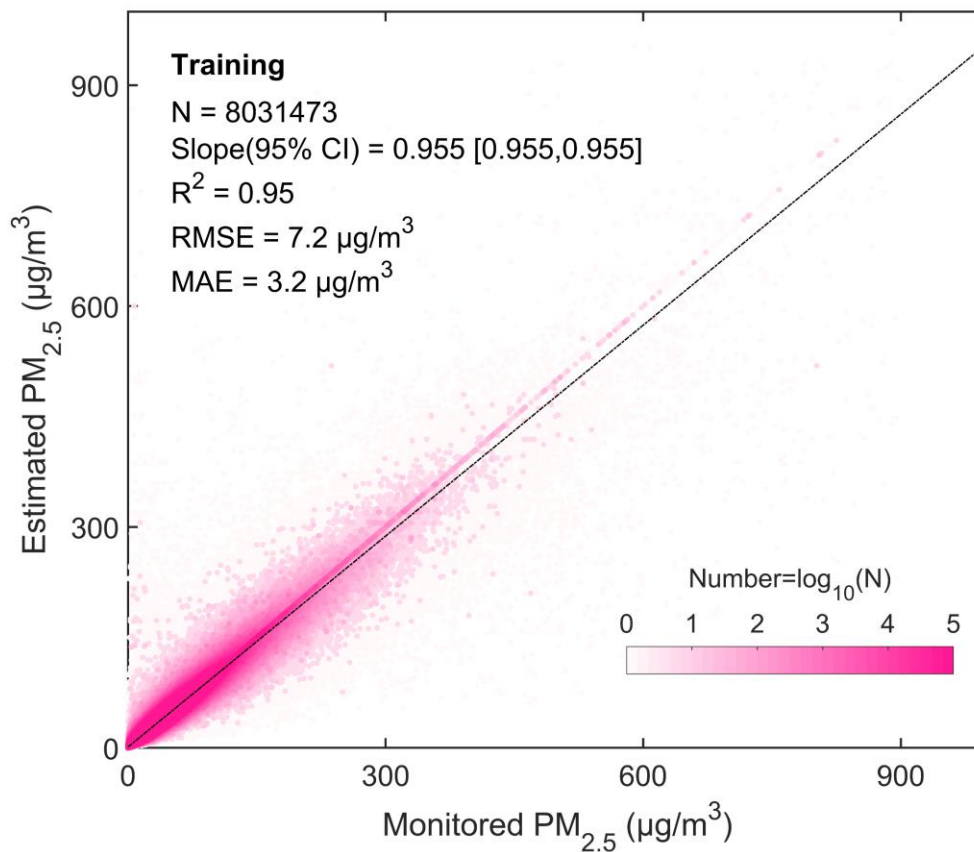


443

444 **Figure 2.** The most important variable (a) and the ranking (b) at all sites. The most important  
 445 variable in each region (c-h). The stacked bar shows the importance rankings of the variables  
 446 ('rank=1' represents the most important variable). The bar shows the proportion of the most  
 447 important variable. The variables are the reciprocal of dry visibility (Vis\_Dry\_In), reciprocal of  
 448 visibility (Vis\_In), temperature (Temp), dew point temperature (Td), temperature-dew point  
 449 difference (Temp-Td), relative humidity (RH), wind speed (WS), numerical time (DateTime) and  
 450 daily number of visibility record (DailyObsNum).

451 **3.2 Evaluation of Model Performance**

452 We analyze the linear regression relationship between all estimated and corresponding response  
 453 values to evaluate the model's performance. Figure 3 is the density scatter plot of the monitored  
 454 PM<sub>2.5</sub> concentration (response values) and the estimated PM<sub>2.5</sub> concentration (estimated values).  
 455 There is a total of 8031473 data pairs for all the sites. The linear regression slope (95% confidence  
 456 interval) is 0.955 [0.955, 0.955], the R<sup>2</sup> is 0.95, the RMSE is 7.2 μg/m<sup>3</sup>, and the MAE is 3.2 μg/m<sup>3</sup>.



457

458 **Figure 3.** Density scatter plot (a) between estimated PM<sub>2.5</sub> concentration and monitored PM<sub>2.5</sub>  
 459 concentration. The dashed black line is the linear regression line. N is the length of the data pairs,  
 460 and Slope is the linear regression coefficient within a 95% confidence interval (CI). R<sup>2</sup> is the  
 461 coefficient of determination, RMSE is the root mean square error, and MAE is the mean absolute  
 462 error.

463 Figure 4 (a-c) shows the spatial distribution (a-c) and frequency of training of RMSE, MAE, and  $\rho$ .  
 464 Table 2 lists the model's performance metrics in the United States, Canada, Europe, China, and India.  
 465 For all sites, the average RMSE is 6.92  $\mu\text{g}/\text{m}^3$ , with a median of 4.76  $\mu\text{g}/\text{m}^3$ . The RMSE of 80%  
 466 of the sites is less than 10.01  $\mu\text{g}/\text{m}^3$ . The RRMSE (the percentage of RMSE to mean of PM<sub>2.5</sub>  
 467 concentration) is 28.7%. The MAE is 3.77  $\mu\text{g}/\text{m}^3$ , with a median of 2.72  $\mu\text{g}/\text{m}^3$ . The MAE is less  
 468 than 5.66  $\mu\text{g}/\text{m}^3$  for 80% of the sites. The RMAE (the percentage of MAE to mean of PM<sub>2.5</sub>  
 469 concentration) is 15.4%. The average  $\rho$  is 0.91, and the median is 0.92. The  $\rho$  of 80% of the sites is  
 470 greater than 0.87. Previous studies have shown that for PM<sub>2.5</sub> concentration retrieved from daily  
 471 visibility or satellite aerosol optical depth, the R<sup>2</sup> range of the model is from 0.42 to 0.89, and the  
 472 RMSE range is from 9.59  $\mu\text{g}/\text{m}^3$  to 32.09  $\mu\text{g}/\text{m}^3$  (Shen et al., 2016; Liu et al., 2017; Wei et al., 2019b;  
 473 Gui et al., 2020; Li et al., 2021; Zhong et al., 2021). This finding indicates that our model performs  
 474 well at the daily scale.

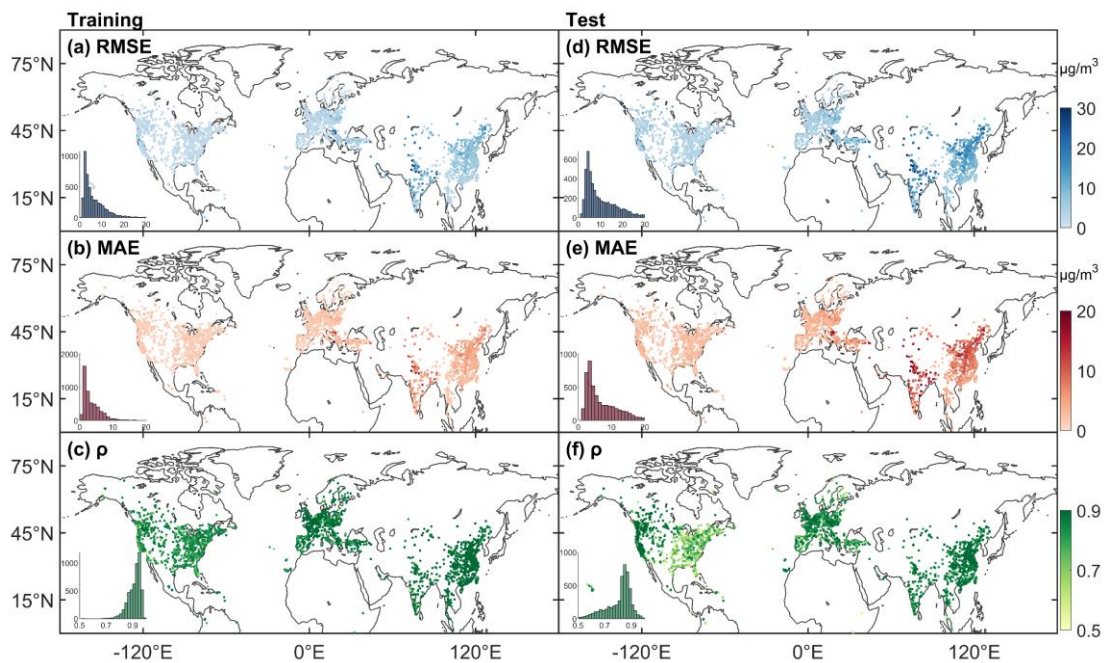
475 On the regional scale, the RMSE values for the United States, Canada, Europe, China, and India are  
 476 3.10  $\mu\text{g}/\text{m}^3$ , 2.78  $\mu\text{g}/\text{m}^3$ , 4.92  $\mu\text{g}/\text{m}^3$ , 9.65  $\mu\text{g}/\text{m}^3$  and 17.46  $\mu\text{g}/\text{m}^3$ , respectively. and the RRMSE  
 477 values are 34.9%, 40.4%, 29.8%, 23.1%, and 28.8%, respectively. The MAEs for the United States,  
 478 Canada, Europe, China, and India are 1.61  $\mu\text{g}/\text{m}^3$ , 1.35  $\mu\text{g}/\text{m}^3$ , 2.54  $\mu\text{g}/\text{m}^3$ , 5.47  $\mu\text{g}/\text{m}^3$ , and 9.13

479  $\mu\text{g}/\text{m}^3$ , respectively. The RMAEs are 17.9%, 19.5%, 16.3%, 13.1%, and 14.4%, respectively. The  $\rho$   
 480 values for the United States, Canada, Europe, China, and India are 0.87, 0.88, 0.91, 0.94, and 0.92,  
 481 respectively. The correlation coefficients are higher in China and India, low in the United States and  
 482 Canada.

483 The largest RMSE and MAE are in India, and the smallest are in Canada. The RRMSE and RMAE  
 484 are larger in the United States, Canada and Europe than in China and India and other regions.

485 **Table 2.** The metrics for all sites and sites in the United States (the US), Canada, Europe, China and  
 486 India. RRMSE is the percentage of RMSE to mean of  $\text{PM}_{2.5}$  concentration. RMAE is the percentage  
 487 of MAE to mean of  $\text{PM}_{2.5}$  concentration.

<i>Region</i>	<i>RMSE</i> ( $\mu\text{g}/\text{m}^3$ )	<i>MAE</i> ( $\mu\text{g}/\text{m}^3$ )	$\rho$	<i>Mean</i> ( $\mu\text{g}/\text{m}^3$ )	<i>RRMSE</i> (%)	<i>RMAE</i> (%)
<i>All</i>	6.92	3.77	0.91	26.7	28.7	15.4
<i>the US</i>	3.10	1.61	0.87	9.1	34.9	17.9
<i>Canada</i>	2.78	1.35	0.88	6.9	40.4	19.5
<i>Europe</i>	4.92	2.54	0.91	15.7	29.8	16.3
<i>China</i>	9.65	5.47	0.94	42.1	23.1	13.1
<i>India</i>	17.46	9.13	0.92	63.1	28.8	14.4
<i>Other</i>	6.11	3.32	0.91	23.4	24.8	14.1

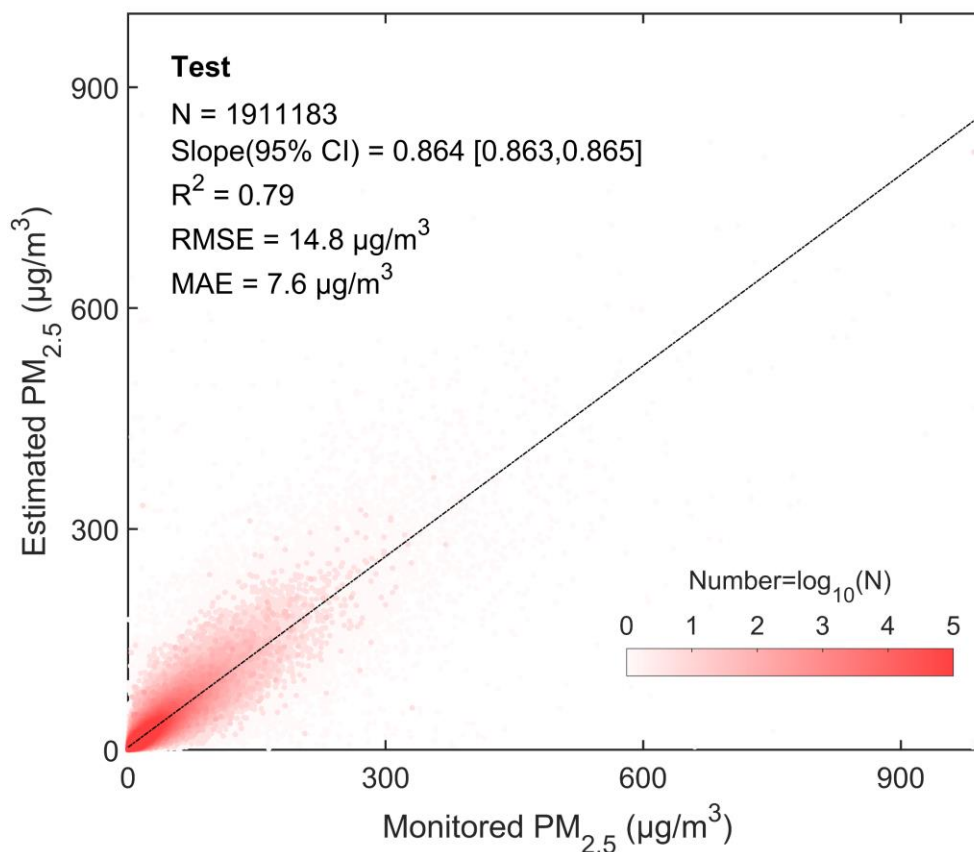


488 **Figure 4.** Statistical Metrics distribution of training (left) and test (right). The bar is the frequency  
 489 of sites. RMSE is the root mean square error, MAE is the mean absolute error, and  $\rho$  is the correlation  
 490 coefficient.  
 491

### 492 3.3 Evaluation of Model's Predictive Ability

493 A total of 1911183 pairs of test data is employed to evaluate the model's predictive ability. Figure 5  
 494 is the density scatter plot between the predicted  $\text{PM}_{2.5}$  concentration and the test  $\text{PM}_{2.5}$  concentration.

495 The linear regression slope (95% CI) is 0.864 [0.863, 0.865],  $R^2$  is 0.79, RMSE is  $14.8 \mu\text{g}/\text{m}^3$ , and  
 496 MAE is  $7.6 \mu\text{g}/\text{m}^3$ . Previous studies have shown that the  $R^2$  range of the model's predictive results  
 497 at the daily scale is 0.31 - 0.84, and the RMSE range is 13.8-29.0  $\mu\text{g}/\text{m}^3$  (Gui et al., 2020; Zhong et  
 498 al., 2021). The test results exhibit excellent predictive capability.



499

500 **Figure 5.** Density scatter plot (a) between the predicted PM<sub>2.5</sub> concentration and monitored PM<sub>2.5</sub>  
 501 concentration of the test results. The dashed black line is the linear regression line. N is the length  
 502 of the data pairs, and Slope is the linear regression coefficient within a 95% confidence interval (CI).  
 503  $R^2$  is the coefficient of determination, RMSE is the root mean square error, and MAE is the mean  
 504 absolute error.

505 We analyze the test results for Canada, the United States, Europe, China, and India to assess the  
 506 predictive ability of the model in different regions. Figure 4 (d - f) shows the spatial distributions of  
 507 the test RMSE, MAE, and  $\rho$  and their frequency. Table 3 lists the test results of the metrics. For all  
 508 sites, the average RMSE is  $11.50 \mu\text{g}/\text{m}^3$ . The RRMSE is 46.0%. The average MAE is  $7.72 \mu\text{g}/\text{m}^3$ .  
 509 The RMAE is 30.7%. The  $\rho$  is 0.81. For the United States, the RMSE, MAE, and  $\rho$  are  $5.06 \mu\text{g}/\text{m}^3$ ,  
 510  $3.25 \mu\text{g}/\text{m}^3$ , and 0.72, respectively. For Canada, the RMSE, MAE, and  $\rho$  are  $4.73 \mu\text{g}/\text{m}^3$ ,  $2.88 \mu\text{g}/\text{m}^3$ ,  
 511 and 0.77, respectively. The results in the United States and Canada are better in the west than in the  
 512 east. The RMSE, MAE, and  $\rho$  for Europe are  $7.79 \mu\text{g}/\text{m}^3$ ,  $5.10 \mu\text{g}/\text{m}^3$ , and 0.80, respectively. For  
 513 China, the RMSE, MAE, and  $\rho$  are  $16.83 \mu\text{g}/\text{m}^3$ ,  $11.50 \mu\text{g}/\text{m}^3$ , and 0.85, respectively. For India, the  
 514 RMSE, MAE, and  $\rho$  are  $27.05 \mu\text{g}/\text{m}^3$ ,  $17.89 \mu\text{g}/\text{m}^3$ , and 0.85, respectively. The results show that in  
 515 developing regions (China and India),  $\rho$  is better than that in developed regions (the United States,  
 516 Canada, and Europe), which means that the predictive ability of the model is better for severely



517 polluted regions.

518 **Table 3.** The test results of the model's performance metrics for all sites and sites in the United  
519 States, Canada, Europe, China and India. RRMSE is the percentage of RMSE to mean of PM<sub>2.5</sub>  
520 concentration. RMAE is the percentage of MAE to mean of PM<sub>2.5</sub> concentration.

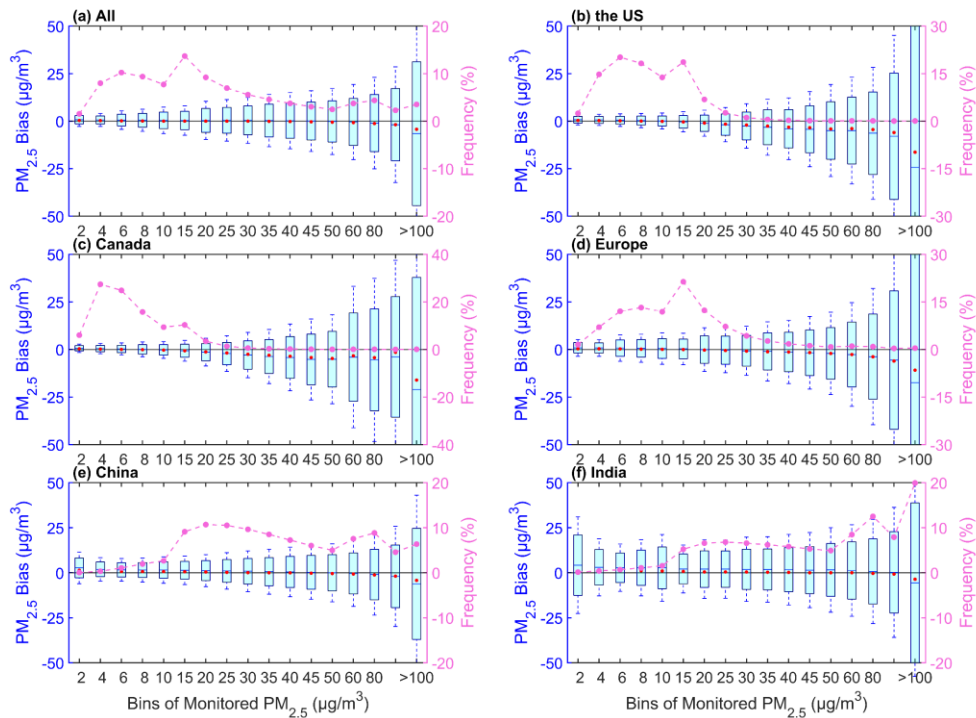
<i>Region</i>	<i>RMSE</i> ( $\mu\text{g}/\text{m}^3$ )	<i>MAE</i> ( $\mu\text{g}/\text{m}^3$ )	$\rho$	<i>Mean</i> ( $\mu\text{g}/\text{m}^3$ )	<i>RRMSE</i> (%)	<i>RMAE</i> (%)
<i>All</i>	11.50	7.72	0.81	27.1	46.0	30.7
<i>the US</i>	5.06	3.25	0.72	9.4	54.3	35.0
<i>Canada</i>	4.73	2.88	0.77	7.2	65.6	40.0
<i>Europe</i>	7.79	5.10	0.80	15.9	47.0	32.0
<i>China</i>	16.83	11.50	0.85	42.6	39.6	27.1
<i>India</i>	27.05	17.89	0.85	63.7	42.9	27.8
<i>Other</i>	8.86	6.16	0.81	23.4	36.7	26.1

### 521 3.4 Uncertainties and Limitations

#### 522 3.4.1 Uncertainty in the Pollution Level

523 Figure 6 shows the uncertainty in the predicted PM<sub>2.5</sub> concentration with respect to the pollution  
524 level of the monitored PM<sub>2.5</sub> concentration. For all sites, the uncertainty in the bias increases as the  
525 pollution level increases. The mean and median of the bias shift from positive to negative with  
526 increasing pollution levels. 83.6% of PM<sub>2.5</sub> concentration data is less than 45  $\mu\text{g}/\text{m}^3$ , and the mean  
527 bias ( $< 0.8 \mu\text{g}/\text{m}^3$ ) is positive. 36.8% is less than 10  $\mu\text{g}/\text{m}^3$ , and the median ( $< 0.4 \mu\text{g}/\text{m}^3$ ) of the bias  
528 is positive. 16.4% of PM<sub>2.5</sub> concentration is great than 45  $\mu\text{g}/\text{m}^3$ , and the mean bias is negative. 63.2%  
529 of PM<sub>2.5</sub> concentration is great than 10  $\mu\text{g}/\text{m}^3$ , and the median is negative. It indicates that the model  
530 overestimates at low pollution level and underestimates at high pollution level.

531 The bias for each region also increases with pollution level. For the United States, the mean bias of  
532 69.4% is positive and less than 0.8  $\mu\text{g}/\text{m}^3$ , and the PM<sub>2.5</sub> concentration is less than 10  $\mu\text{g}/\text{m}^3$ . When  
533 the PM<sub>2.5</sub> concentration is greater than 10  $\mu\text{g}/\text{m}^3$ , the mean bias is negative. For Canada, the mean  
534 bias of 74.1% is positive and less than 0.7  $\mu\text{g}/\text{m}^3$ . When the PM<sub>2.5</sub> concentration is greater than 8  
535  $\mu\text{g}/\text{m}^3$ , the mean bias is negative. For Europe, the mean bias of 67.1% is positive and less than 0.9  
536  $\mu\text{g}/\text{m}^3$ . When the PM<sub>2.5</sub> concentration is greater than 15  $\mu\text{g}/\text{m}^3$ , the mean bias is negative. For China,  
537 67.7% of the bias is positive and less than 2.7  $\mu\text{g}/\text{m}^3$ . When the PM<sub>2.5</sub> concentration is greater than  
538 45  $\mu\text{g}/\text{m}^3$ , the mean bias is negative. For India, 80.1% of the bias is positive and less than 4.2  $\mu\text{g}/\text{m}^3$ ,  
539 and when the PM<sub>2.5</sub> concentration is greater than 100  $\mu\text{g}/\text{m}^3$ , the mean bias is negative. When the  
540 PM<sub>2.5</sub> concentration is greater than 60  $\mu\text{g}/\text{m}^3$ , the bias median is negative, with a percentage of  
541 40.3%. The uncertainty in each region is similar, and the uncertainty increases as the pollution level  
542 increases.



543

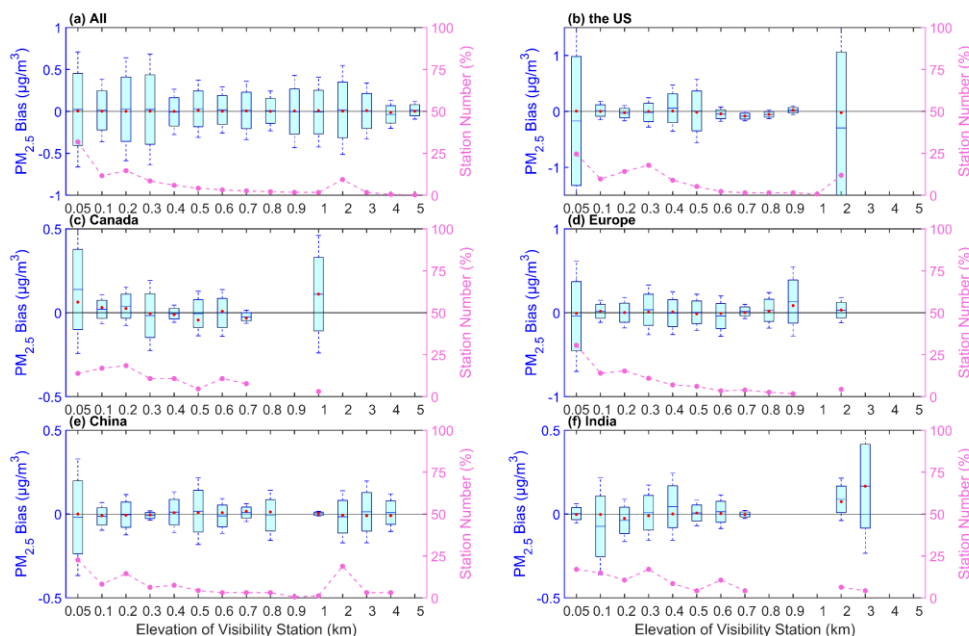
544 **Figure 6.** Boxplots of the pollution level and bias (predicted  $PM_{2.5}$  concentration - monitored  $PM_{2.5}$   
 545 concentration) for all sites (a), sites in the United States (b), Canada (c), Europe (d), China (e), and  
 546 India (f). The box's upper and lower limits represent  $\pm 1$  standard deviation, the whiskers represent  
 547 2 times the standard deviation, the red circle represents the median, and the short line represents the  
 548 mean bias. The frequency (%) on the right y-axis represents the percentage of data with different  
 549 pollution levels (dashed line).

### 550 3.4.2 Uncertainty in the Station Elevation

551 With the spatial variability in  $PM_{2.5}$  concentration, we analyze the mean bias at different visibility  
 552 station elevations. Figure 7 shows the relationships between the elevations of the visibility stations  
 553 and the bias. The bias exhibits variations across different elevations for all stations. The mean bias  
 554 of all sites ranges from  $-0.04$  to  $0.02 \mu\text{g}/\text{m}^3$ . A total of 90.1% of the stations has positive biases. The  
 555 median of the bias is almost positive, with a positive bias of 99.5% stations, except for the elevation  
 556 at 4 km. The elevations of 86.5% of the stations are less than 1 km, with a positive median of the  
 557 bias. High uncertainties in bias occur at elevations of 0.05 km, 0.2 km, and 0.3 km. Negative biases  
 558 are observed at elevations of 0.4 km, 0.9-1 km, and 4 km. This finding indicates a nonsignificant  
 559 overestimation of the predicted  $PM_{2.5}$  concentration due to the various elevations.

560 The bias patterns vary across regions. For the United States, a total of 88.8% of the stations have  
 561 negative biases. The median of the bias is negative with a percentage of 63.4%. High uncertainties  
 562 in bias occur at elevations of 0.05 km, 2 km, and 0.3 km. For Canada, 52.3% of the stations have  
 563 positive biases. The median of the bias is negative with a percentage of 33.8%. High uncertainties  
 564 in bias occur at elevations of 0.05 km and 1 km. For Europe, 58.9% of the stations have positive  
 565 biases. The median of the bias is negative with a percentage of 40.2%. High uncertainties in bias  
 566 occur at elevations of 0.05 km and 0.9 km. For China, 76.7% of the stations have negative biases.

567 The median of the bias is negative with a percentage of 54.1%. High uncertainties in bias occur at  
 568 elevations of 0.05 km, 0.5 km and 3 km. For India, 68.1% of the stations have positive biases. The  
 569 median of the bias is negative with a percentage of 63.8%. The elevation of most stations with a  
 570 high uncertainty is at 0.05 km. High uncertainties in bias occur at elevations of 0.1 km and 3 km.  
 571 More stations with negative bias are in the United States and China. More stations with positive bias  
 572 are in Canada, Europe and India.



573

574 **Figure 7.** Boxplots of the bias (predicted PM<sub>2.5</sub> concentration - monitored PM<sub>2.5</sub> concentration) and  
 575 the elevation of the visibility station for all sites (a), sites in the United States (b), Canada (c),  
 576 Europe (d), China (e), and India (f). The box's upper and lower limits represent  $\pm 1$  standard deviation,  
 577 the whiskers represent 2 times the standard deviation, the red circle represents the median, and the short  
 578 line represents the mean bias. The station number (%) on the right y-axis represents the percentage  
 579 of station number at different elevations (dashed line).

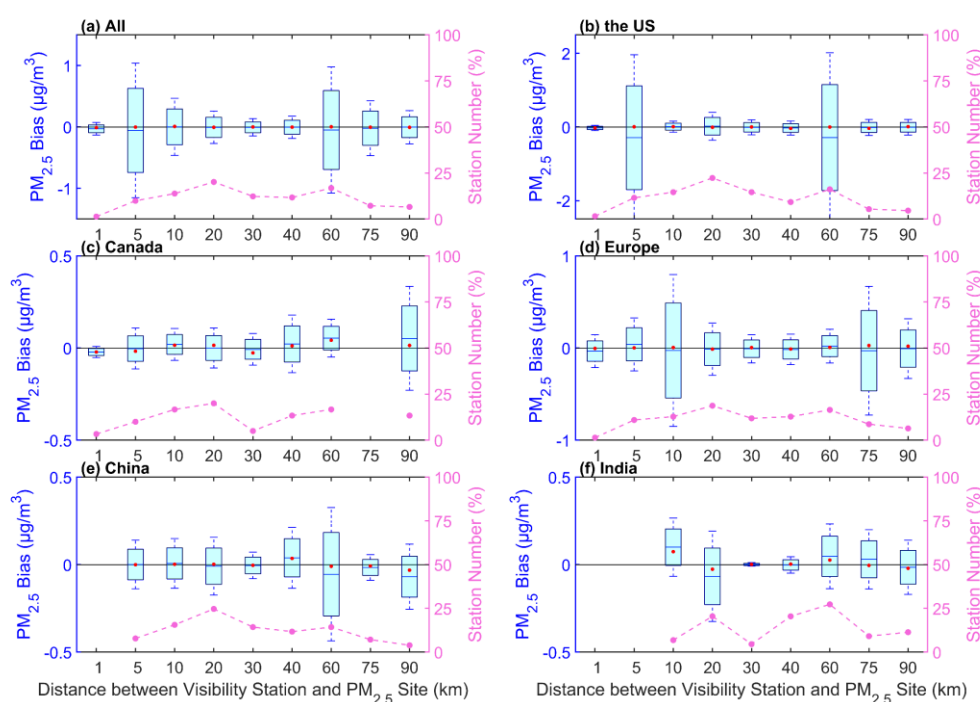
### 580 3.4.3 Uncertainty in the Station Distance

581 As the visibility stations and PM<sub>2.5</sub> sites are not collocated, we analyze the mean bias of PM<sub>2.5</sub>  
 582 concentration at different distances, as shown in Figure 8. For all sites, 86.1% of the stations have  
 583 negative biases. The median of the bias is negative with a percentage of 70.8%. More stations have  
 584 a negative bias caused by the distance. The uncertainty has no signification with the distance. The  
 585 distances with low uncertainties are at 1 km and 20-40 km. The distances with high uncertainties  
 586 are at 5 km and 60 km.

587 For the United States, 63.1% of the stations have negative biases. The median of the bias is negative  
 588 with a percentage of 69.2%. The distance with the lowest uncertainty is at 1 km. The distances with  
 589 high uncertainties are at 5 km and 60 km. For Canada, 60.0% of the stations have positive biases.  
 590 The median of the bias is positive with a percentage of 80.0%. The uncertainty shows an increase  
 591 with the distance increasing. For Europe, 72.7% of the stations have negative biases. The median of  
 592 the bias is positive with a percentage of 67.1%. When the distance is less than 10 km, the uncertainty

593 increases with the distance. The distances with low uncertainties are at 1 km and 30-40 km. The  
 594 distances with high uncertainties are at 10 km and 75 km. For China, 64.3% of the stations have  
 595 negative biases. The median of the bias is negative with a percentage of 72.7%. The distance with a  
 596 low uncertainty is at 30 km. The distance with a high uncertainty is at 60 km. For India, 62.3% of  
 597 the stations have negative biases. The median of the bias is positive with a percentage of 59.1%.  
 598 The distance with the lowest uncertainty is at 30 km. The distance with the highest uncertainty is at  
 599 20 km.

600 More visibility stations have negative biases, except for the stations in Canada. For the stations in  
 601 the United States, Canada and Europe, the lowest uncertainty is at 1 km. For the stations in China  
 602 and India, the uncertainty has no significant relationship with distance, though the distance has  
 603 caused a negative bias.



604

605 **Figure 8.** Boxplots of the mean bias (predicted PM<sub>2.5</sub> concentration - monitored PM<sub>2.5</sub> concentration)  
 606 and the distance between the visibility station and the PM<sub>2.5</sub> site and for all sites (a), sites in the  
 607 United States (b), Canada (c), Europe (d), China (e), and India (f). The box's upper and lower limits  
 608 represent ±1 standard deviation, the whiskers represent 2 times the standard deviation, the red circle  
 609 represents the median, and the short line represents the mean bias. The station number (%) on the  
 610 right y-axis represents the percentage of station number under different distances (dashed line).

### 611 3.4.4 Discussion on the Uncertainties and Limitations

612 There are some uncertainties and limitations in this study. The upper limit of visibility and PM<sub>2.5</sub>  
 613 concentration can cause some uncertainties in model training. The maximum distance between the  
 614 visibility stations and PM<sub>2.5</sub> monitoring sites is 100 km due to the spatial variability in aerosols,  
 615 which may increase the uncertainty in the estimated PM<sub>2.5</sub> concentration. Because of the nonuniform  
 616 vertical distribution of aerosols, the different elevations of the visibility stations and the PM<sub>2.5</sub>  
 617 monitoring sites further increase the uncertainty in estimating PM<sub>2.5</sub> concentration. In addition, the

618 spatial coverage of visibility stations, especially in China and India, is still limited, which may  
619 increase the uncertainty in the representativeness of regional PM<sub>2.5</sub> concentration and pollution  
620 levels. With the increasing human concern of air pollution and the implementation of air pollution  
621 control measures, the types of major atmospheric pollutants may have changed at regional scale, the  
622 composition of particulate matter has also evolved, the scattering and absorption characteristics may  
623 have changed, and the relationship between visibility and PM<sub>2.5</sub> concentration may change. These  
624 changes may lead to uncertainties in estimating historical PM<sub>2.5</sub> concentration. It is challenging to  
625 validate by ground observations and satellite-based estimation prior to 2000. Despite these  
626 limitations and challenges, we establish a long-term PM<sub>2.5</sub> concentration dataset based on visibility  
627 from 1959 to 2022, which has been carefully validated and evaluated, providing insights into the  
628 long-term spatiotemporal characteristics of concentration PM<sub>2.5</sub> in the Northern Hemisphere.

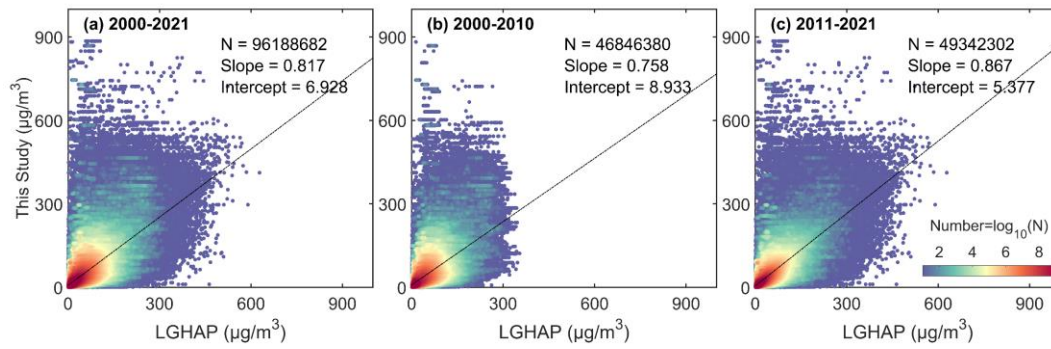
#### 629 **4 Comparisons with Other PM<sub>2.5</sub> Concentration Dataset**

630 We compare the daily and monthly estimated PM<sub>2.5</sub> concentration with the LGHAP PM<sub>2.5</sub>  
631 concentration from 2000 to 2021 to further demonstrate the reliability the estimated PM<sub>2.5</sub>  
632 concentration. When comparing on the regional scale, we split the time range into 2000-2010 and  
633 2011-2021, to further validate the accuracy and consistency of estimated PM<sub>2.5</sub> concentrations, as  
634 in some regions such as India and China, there are almost no continuous PM<sub>2.5</sub> monitoring data  
635 before 2010.

#### 636 **4.1 Comparisons on the Daily Scale**

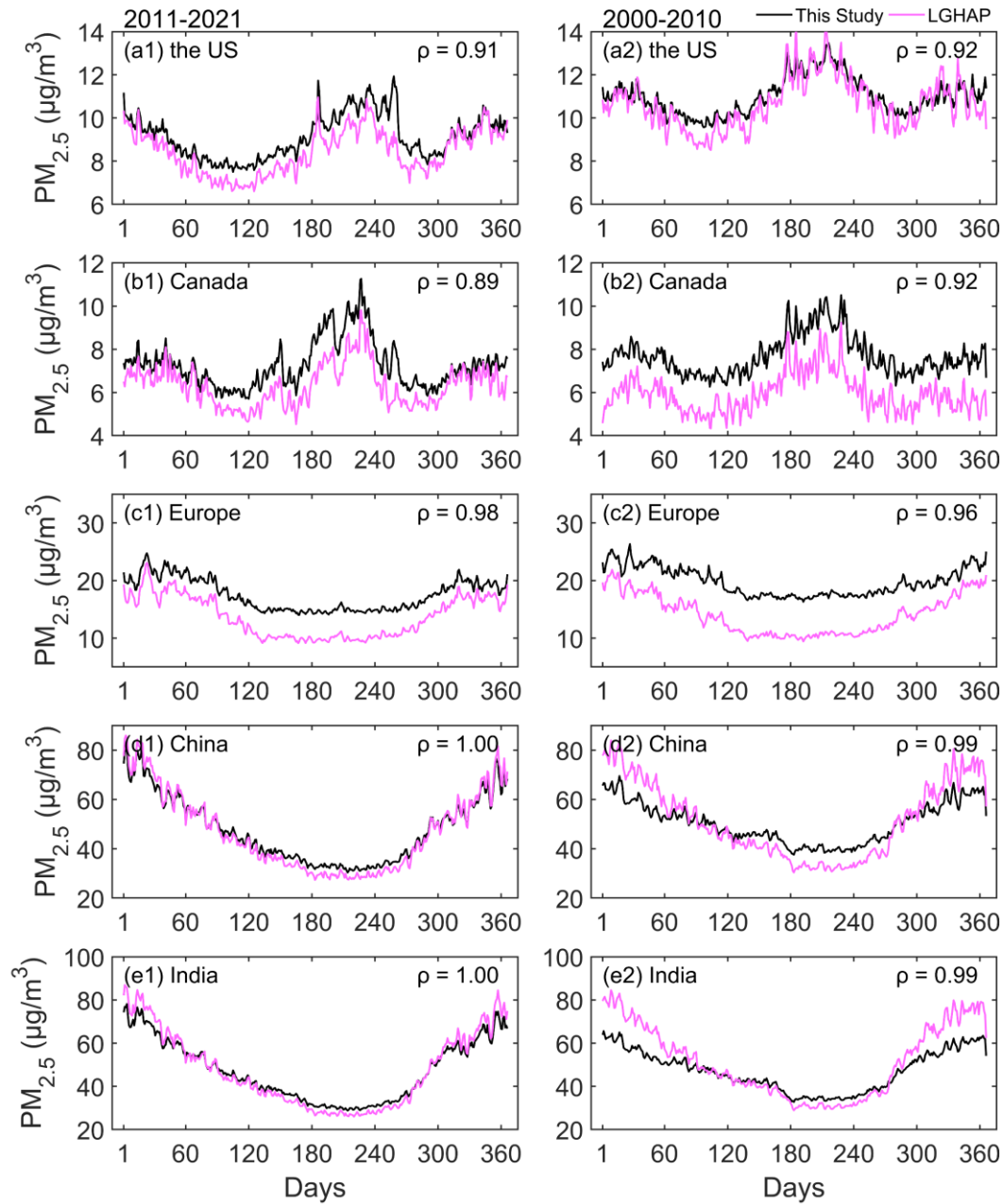
637 We spatiotemporally match the LGHAP PM<sub>2.5</sub> concentration with the estimated PM<sub>2.5</sub> concentration.  
638 Figure 9 shows the density scatter plot between the estimated PM<sub>2.5</sub> concentration and LGHAP  
639 PM<sub>2.5</sub> concentration. There is a total of 96188682 pairs during the period of 2000 and 2021,  
640 46846389 pairs during the period from 2000 to 2010, and 49342302 during the period of 2011 and  
641 2021, with slopes of 0.817, 0.758 and 0.867. The intercepts are 6.928 µg/m<sup>3</sup>, 8.933 µg/m<sup>3</sup>, and 5.377  
642 µg/m<sup>3</sup>, respectively. The slope decreases before 2010, which may be related to the upper limit of  
643 LGHAP PM<sub>2.5</sub> concentration with a significantly decreasing quantity of the concentration (> 300  
644 µg/m<sup>3</sup>).

645 We further compare the PM<sub>2.5</sub> concentrations of the annual calendar cycles on the regional scale in  
646 Figure 10. The PM<sub>2.5</sub> concentration of each day is the mean of the PM<sub>2.5</sub> concentrations at all sites  
647 in the region. The correlation coefficients of the PM<sub>2.5</sub> concentrations are greater than 0.89 from  
648 2011 to 2021 and greater than 0.92 from 2000 to 2010. The correlation is greater in Europe, China,  
649 and India than in the United States and Canada. There is no significant difference in the variation of  
650 annual calendar cycles between two periods on the regional scale. In the United States, PM<sub>2.5</sub>  
651 concentration between 2000 and 2010 is more similar than the concentration between 2011 and  
652 2021, and the bias decreases. In Canada, the correlation coefficient increases, although the bias  
653 increases. In Europe, the correlation coefficient and bias increase. There are similar changes in  
654 China and India. The bias increases on days 1 to 60 and 300 to 366, but the correlation remains  
655 significant. The difference of PM<sub>2.5</sub> concentration during the two periods is mainly reflected in the  
656 increasing bias in Canada and Europe, which is a non-seasonal bias and the increasing bias in winter  
657 in China and India, which is a seasonal bias. Overall, PM<sub>2.5</sub> concentrations show a good consistency  
658 before and after 2010 on the daily scale.



659

660 **Figure 9.** Density scatter plot between the estimated PM<sub>2.5</sub> concentration (this study) and LGHAP  
 661 PM<sub>2.5</sub> concentration on the daily scale from 2000 to 2021 (a), from 2000 to 2010 (b) from 2011 to  
 662 2021. The dashed black line is the linear regression line. N is the length of the data pairs, and Slope  
 663 is the linear regression coefficient. Intercept represents the y-intercept.



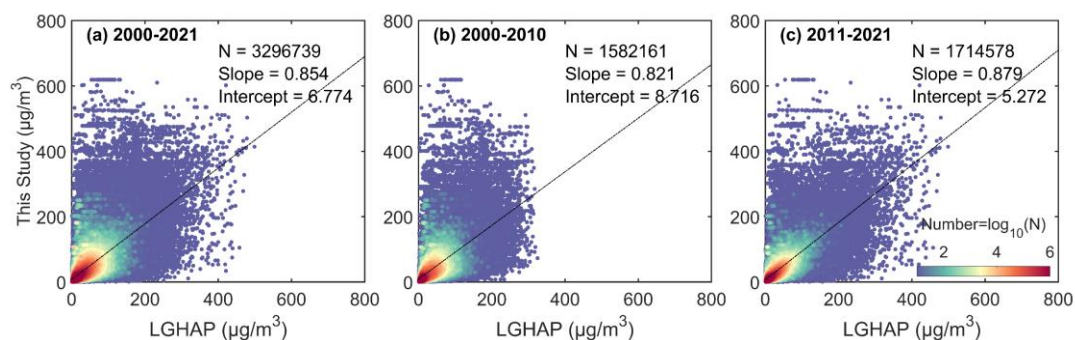
664

665 **Figure 10.** Comparison of annual calendar cycle of  $PM_{2.5}$  concentration on the regional scale from  
 666 2011 to 2021 (left) and from 2000 to 2010 (right) between the estimated  $PM_{2.5}$  concentration (this  
 667 study) and LGHAP  $PM_{2.5}$  concentration on the daily scale.  $\rho$  is the correlation coefficient.

668 **4.2 Comparisons on the Monthly Scale**

669 Figure 11 shows the density scatter plot between the estimated  $PM_{2.5}$  concentration and LGHAP  
 670  $PM_{2.5}$  concentration on the monthly scale. The monthly  $PM_{2.5}$  concentration is calculated by the  
 671 matched daily concentrations. There is a total of 3296739 pairs during the period from 2000 to 2021,  
 672 1582161 pairs during the period from 2000 to 2010, and 1714578 during the period from 2011 to  
 673 2021, with slopes of 0.857, 0.821 and 0.879. The intercepts are 6.774  $\mu\text{g}/\text{m}^3$ , 8.716  $\mu\text{g}/\text{m}^3$ , and 5.272  
 674  $\mu\text{g}/\text{m}^3$ , respectively. The slope of monthly concentration significantly improves before 2010, and  
 675 slightly increases after 2010 compared to the daily scale.

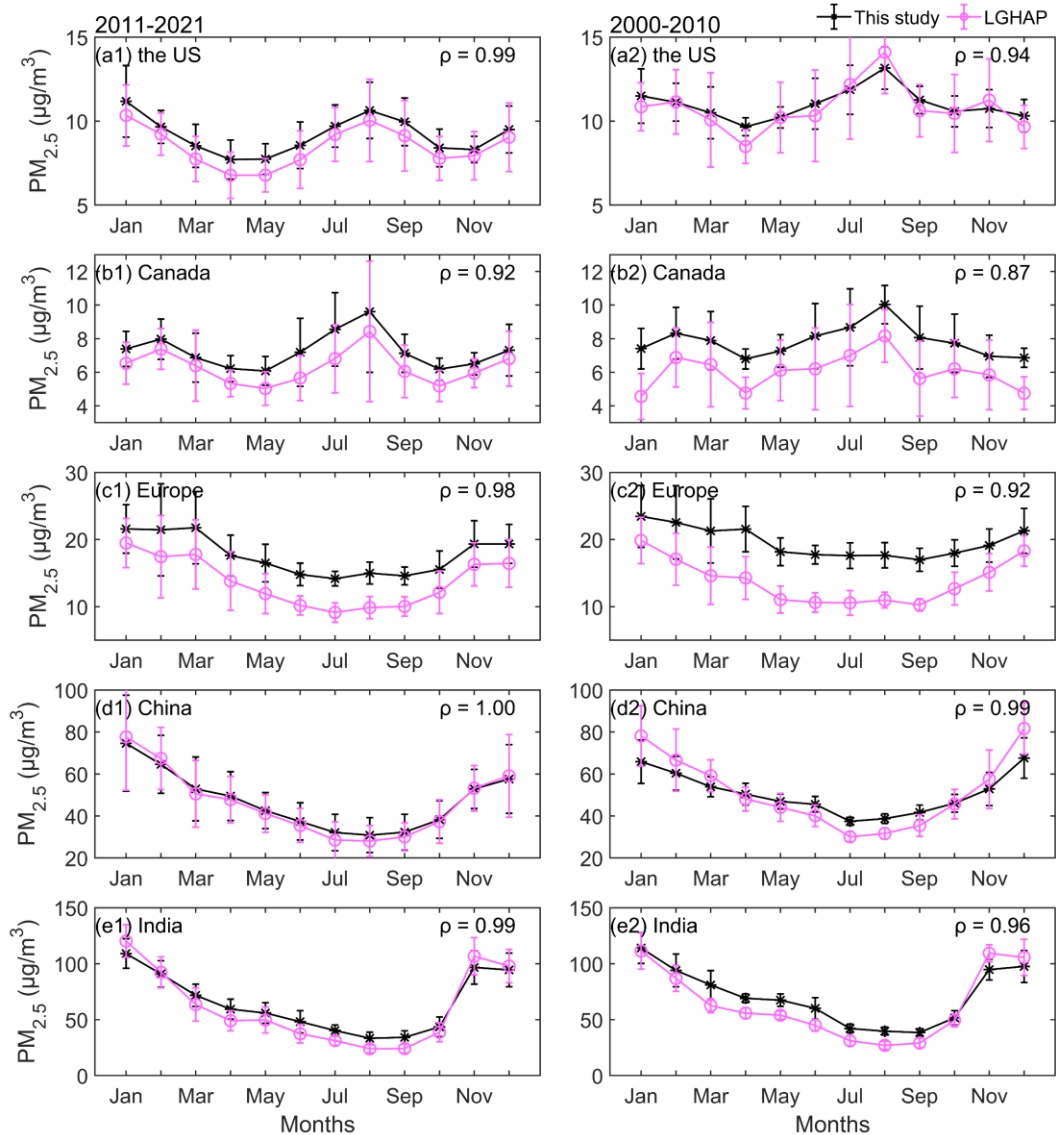
676 We also compare the  $PM_{2.5}$  concentrations of the annual cycles on the regional scale in Figure 12.  
 677 The  $PM_{2.5}$  concentration of each month is the mean of the  $PM_{2.5}$  concentrations at all sites in the  
 678 region. The correlation coefficients of the  $PM_{2.5}$  concentrations are greater than 0.92 from 2011 to  
 679 2021 and greater than 0.87 from 2000 to 2010. In the United States, the  $PM_{2.5}$  concentrations before  
 680 2010 are closer compared to those after 2010, except in April and August, and the biases in other  
 681 months has significantly decreased. In Europe and Canada, the biases have increased. In China, the  
 682 result is similar with the result on the daily scale. In India, the performance of the two is almost  
 683 consistent, with a correlation coefficient of 0.99 and 0.96. The two datasets have a very high  
 684 similarity in annual cycles, indicating that the estimated  $PM_{2.5}$  concentration in this study is accurate  
 685 and consistent before and after 2010.



686

687 **Figure 11.** Density scatter plot between the estimated  $PM_{2.5}$  concentration (this study) and LGHAP  
 688  $PM_{2.5}$  concentration on the monthly scale from 2000 to 2021 (a), from 2000 to 2010 (b) from 2011  
 689 to 2021. The dashed black line is the linear regression line. N is the length of the data pairs, and  
 690 Slope is the linear regression coefficient. Intercept represents the y-intercept.





691

692 **Figure 12.** Comparison of annual cycle of monthly  $PM_{2.5}$  concentration on the regional scale from  
 693 2011 to 2021 (left) and from 2000 to 2010 (right) between the estimated  $PM_{2.5}$  concentration (this  
 694 study) and LGHAP  $PM_{2.5}$  concentration on the daily scale.  $\rho$  is the correlation coefficient.

695 **4.3 Discussion on the Differences of  $PM_{2.5}$  Concentration from Visibility and Aerosol Optical**  
 696 **Depth**

697 Both visibility and aerosol optical depth are excellent alternatives for estimating  $PM_{2.5}$  concentration,  
 698 with its own advantages. However, they have differences in principle, which may be the reason for  
 699 the difference between the two datasets in comparison.

700 Fine particulate matter near the ground surface affects atmospheric visibility through scattering.  
 701 Studies have shown visibility has a negative correlation with  $PM_{2.5}$  concentration, and the reciprocal  
 702 of visibility has a positive correlation with the extinction coefficient and has a negative correlation  
 703 with the particulate matter concentration (Wang et al., 2012; Zhang et al., 2017; Zhang et al., 2020).  
 704 Therefore, visibility is often used as a proxy for particulate matter pollution (Huang et al., 2009;  
 705 Singh et al., 2020) and it is the basis to estimate  $PM_{2.5}$  concentration. In addition, studies have shown

706 that meteorological observations such as temperature and humidity also play an important role in  
707 estimating PM<sub>2.5</sub> concentration using visibility (Shen et al., 2016; Xue et al., 2019; Zhong et al.,  
708 2021). Therefore, when estimating PM<sub>2.5</sub> concentration based on visibility data, only conventional  
709 meteorological variables need to be added, which is convenient and accurate observational data.  
710 Besides, the long-term, complete and high-temporal ground-based observations are the advantage  
711 of historical estimation of PM<sub>2.5</sub> concentration. The daily mean from continuous or equidistant  
712 hourly observations greatly increases the daily representativeness.

713 The aerosol optical depth is a physical quantity that describes aerosol column properties, which is  
714 the integration of the extinction coefficient in the vertical direction. When establishing a connection  
715 between aerosol optical depth and near-ground PM<sub>2.5</sub> concentration, it is essential to consider the  
716 vertical structure of aerosols. Studies have shown that the aerosol vertical profiles usually are  
717 provided by observations, assumptions, or chemical transport models to obtain the aerosol  
718 properties near the surface (Van Donkelaar et al., 2010; Wei et al., 2019b; Van Donkelaar et al.,  
719 2021). Van Donkelaar et al. (2006; 2010) have demonstrated that aerosol vertical profile errors in  
720 chemical transport models and aerosol optical depth retrieval and sampling result in an  
721 approximately 25% uncertainty of one standard deviation. Sensitivity testing shows that a 1%  
722 estimation error in the aerosol optical depth can lead to a 0.27% estimation error in the PM<sub>2.5</sub>  
723 concentration (Wei et al., 2021). Besides, the retrieval of aerosol optical depth is affected by clouds  
724 or surface types and a finite number of daily observations (usually 1-2 times), though it has the  
725 advantage of high spatial coverage (Liu et al., 2017; Singh et al., 2020; Zhong et al., 2021).

726 Another difference is the upper limit of PM<sub>2.5</sub> concentration. In this study, the upper limit of the  
727 estimated daily PM<sub>2.5</sub> concentration is set to 1000 µg/m<sup>3</sup> (the same for input data). When the PM<sub>2.5</sub>  
728 concentration is greater than 500 µg/m<sup>3</sup> during heavy pollution, which may contribute to the higher  
729 frequency at high pollution levels than in the LGHAP dataset, especially before 2010. We do not  
730 remove visibility records during dust weather when preprocessing the data, which may lead to an  
731 overestimation of PM<sub>2.5</sub> concentration in dusty areas, such as northern China and northwestern India.  
732 In section 3.4, the uncertainty analysis has provided an explanation for the overestimation. Overall,  
733 our PM<sub>2.5</sub> concentration dataset has a good consistency with PM<sub>2.5</sub> concentration based on aerosol  
734 optical depth.

## 735 **5 Regional Trends and Spatial Patterns**

736 We use the estimated PM<sub>2.5</sub> concentrations (at least 10-day records in a site) to calculate monthly  
737 PM<sub>2.5</sub> concentrations, and analyze the annual cycles, interannual trends, and spatial patterns of PM<sub>2.5</sub>  
738 concentrations in different regions based on the GAMM model. The annual variation comes from  
739 the monthly smooth term of GAMM, the interannual variation comes from the annual smooth term,  
740 and the spatial pattern comes from the spatial smooth term. The regions include Canada, the United  
741 States, Europe, China, and India. The results are shown in Figure 13. The trend from 1959 to 2022  
742 in each region is the slope of the Sen-Theil (ST Slope) estimators (Sen, 1968; Theil, 1992), and  
743 Mann-Kendall test (Mann, 1945; Kendall, 1948) is used to calculate the significance of the trend.  
744 The test results show the p-values are all less than 0.01 in all regions.

745 In the United States, the annual cycle curve shows that the PM<sub>2.5</sub> concentration is a 'double peaks  
746 and double valleys' shape. The peaks occur in July and December, respectively, with the highest  
747 PM<sub>2.5</sub> concentration in July throughout the year. The valley values are in April and October, and the

748 PM<sub>2.5</sub> concentration levels are equivalent. The trend is -0.40 µg/m<sup>3</sup>/decade, and PM<sub>2.5</sub> concentration  
749 decreases significantly after 1992, with a trend of -1.39 µg/m<sup>3</sup>/decade. The high PM<sub>2.5</sub> concentration  
750 areas are in the east and west. The areas with low PM<sub>2.5</sub> concentrations are mainly located in the  
751 central and northern regions. The high concentration in the eastern and western regions is related to  
752 extensive industrial activities and densely populated cities. The low concentration in the central and  
753 northern regions is relatively to high vegetation coverage, low industrial activity and low population  
754 density.

755 In Canada, the annual cycle curve also shows that the PM<sub>2.5</sub> concentration is a 'double peaks and  
756 double valleys' shape. The peak values occur in August and February, with the highest PM<sub>2.5</sub>  
757 concentration in August. The valley values are in April and October. The trend is -0.10 µg/m<sup>3</sup>/decade,  
758 and PM<sub>2.5</sub> concentration increases after 2010. The PM<sub>2.5</sub> concentration exhibits an east-high to west-  
759 low pattern. The eastern regions, such as Ontario and Quebec, are characterized by high population  
760 density and significant industrial and transportation activities.

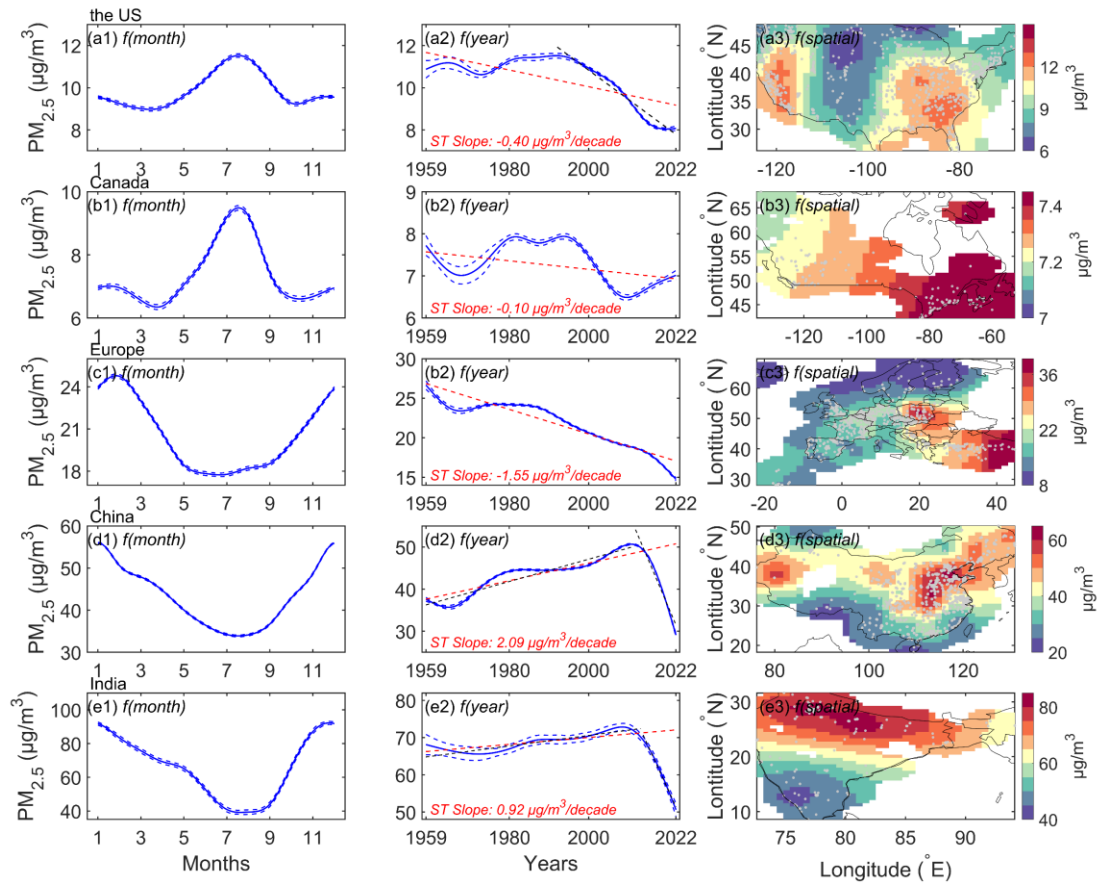
761 In Europe, the annual cycle of PM<sub>2.5</sub> concentration shows that the PM<sub>2.5</sub> concentration is the highest  
762 in February, and is low from May to September. The valley values are in April and October. The  
763 trend is -1.55 µg/m<sup>3</sup>/decade. High concentration areas are distributed in eastern Europe, while low  
764 concentration areas are in northern and western Europe. Eastern Europe exhibits more  
765 industrialization, particularly with a prevalence of traditional heavy industries and the use of coal  
766 and other high-pollution energy sources. In contrast, the energy structure in western Europe tends  
767 to favor cleaner energy sources.

768 In China, the annual cycle curve of PM<sub>2.5</sub> concentration presents a V-liked shape. It indicates that  
769 high concentrations are in winter, while low concentrations are in summer. The trend is 2.09  
770 µg/m<sup>3</sup>/decade. The trend is 2.65 µg/m<sup>3</sup>/decade from 1959 to 2011 and -22.23 µg/m<sup>3</sup>/decade from  
771 2012 to 2022. High concentration areas are distributed in northern China, such as North China Plain,  
772 Northeast China, Sichuan Basin, Taklimakan Desert, and Badain Jaran Desert. Low concentration  
773 areas are in southern China and Northern Tianshan Mountains. Besides dust, industrial activities  
774 and coal combustion for heating during winter are significant contributors to the PM<sub>2.5</sub> concentration  
775 in northern regions.

776 In India, the annual cycle curve of PM<sub>2.5</sub> concentration also presents a V-liked shape. High  
777 concentrations are in winter, and low concentrations are in summer. The trend is 0.92 µg/m<sup>3</sup>/decade.  
778 The trend is 1.41 µg/m<sup>3</sup>/decade from 1959 to 2013 and -23.36 µg/m<sup>3</sup>/decade from 2014 to 2022.  
779 Some studies have shown that the PM<sub>2.5</sub> concentration in India has decreased since 2014, especially  
780 in northern cities. Singh et al. (2021) have found that five major cities in India show a downward  
781 trend from 2014 to 2019, with the largest decline of approximately -4.2 µg/m<sup>3</sup> per year in New Delhi.  
782 Ravindra et al. (2024) also finds that the trend in New Delhi is about -5 µg/m<sup>3</sup> per year from 2014  
783 to 2020. These studies have shown a faster downward trend than our study, as these PM<sub>2.5</sub>  
784 monitoring sites are mainly concentrated in urban areas. The PM<sub>2.5</sub> concentration exhibits a north-  
785 high to south-low pattern. High concentration areas are distributed in northern India, such as Ganges  
786 Plain and Thar Desert, because there are more industrial and densely populated areas and the terrain  
787 leads to the retention of air pollutants. Low concentration areas are in Deccan Plateau.

788 Above all, the PM<sub>2.5</sub> concentrations in developed countries and regions are significantly lower than  
789 those in developing countries in the Northern Hemisphere. Regional trends are similar with those

790 of previous studies in different periods (Van Donkelaar et al., 2010; Wang et al., 2012; Boys et al.,  
791 2014; Ma et al., 2016; Li et al., 2017; Hammer et al., 2020). The trends in PM<sub>2.5</sub> concentration  
792 changes in different regions are closely associated with the implementation of relevant policies. The  
793 earlier pollution control measures are taken, the earlier the decreasing trend in the PM<sub>2.5</sub>  
794 concentration occurs, and the lower the threat of particulate matter pollution is to humans. In 1997,  
795 the United States EPA classified PM<sub>2.5</sub> as a hazardous substance in the National Ambient Air Quality  
796 Standard, and subsequent regulations in 2006 further strengthened the source control and  
797 management of fine particulate matter (Hall and Gilliam, 2016). In 1988, the Canadian federal  
798 government enacted the Canadian Environmental Protection Act, which enhanced the regulation of  
799 PM<sub>2.5</sub> (Davies, 1988). The European Union introduced the Air Quality Directive in 1996, followed  
800 by multiple revisions and updated to regulate and restrict air pollutants, including PM<sub>2.5</sub> (Kuklinska  
801 et al., 2015). However, Europe stands out due to its early adoption of clean production practices in  
802 heavy industries since the 1970s. Since 2012, China has implemented numerous regulations and  
803 standards for PM<sub>2.5</sub>. For instance, the Monitoring Method for Atmospheric Particulate Matter (PM<sub>2.5</sub>)  
804 was issued in 2012, and the Chinese Ministry of Environmental Protection released the Ambient Air  
805 Quality Standards in 2013, including emission standards for PM<sub>2.5</sub> (Zhao et al., 2016a). In 2009, the  
806 Indian Ministry of Environment and Forests issued the National Ambient Air Quality Standards,  
807 which include control standards for PM<sub>2.5</sub>. Since 2015, the Indian government has launched the  
808 National Clean Air Programme (NCAP) to improve air quality by implementing a series of measures  
809 to reduce the emissions of PM<sub>2.5</sub> and other pollutants (Ganguly et al., 2020). These environmental  
810 regulations have contributed significantly to the decline of PM<sub>2.5</sub> concentrations. Some studies have  
811 shown that the variation of PM<sub>2.5</sub> concentrations is also related to several factors, such as the energy  
812 structure, urbanization process, population distribution and vegetation coverage (Shi et al., 2018;  
813 Wu et al., 2018; Li et al., 2019; Wang et al., 2019; Lim et al., 2020; Qi et al., 2023).



814

815 **Figure 13.** Annual cycles, interannual trends and spatial patterns of PM<sub>2.5</sub> concentrations in the  
 816 United States (a1-a3), Canada (b1-b3), Europe (c1-c3), China (d1-d3), and India (e1-e3). The left  
 817 column 'f(month)' is the annual cycle, the middle column 'f(year)' is the interannual trend, and the  
 818 right column 'f(spatial)' is the spatial distribution from Generalized Additive Mixed Model  
 819 (GAMM). The blue dashed lines represent  $\pm 1$  standard error of the month and annual mean of PM<sub>2.5</sub>  
 820 concentrations. The red or black dashed lines represent the trends of the Sen-Theil estimators (ST  
 821 Slope). Mann-Kendall test of trends shows that the p-values are less than 0.01 in all regions. The  
 822 scatter points in right column are the locations of PM<sub>2.5</sub> monitoring sites.

## 823 6 Conclusions

824 In this study, we use a machine learning method to estimate daily PM<sub>2.5</sub> concentration for 5023  
 825 terrestrial sites in the Northern Hemisphere from 1959 to 2022 based on daily visibility and related  
 826 meteorological variables. The first 80% of PM<sub>2.5</sub> concentration data in each site are used to train the  
 827 model, and the last 20% are used to test. The model's performance and predictive ability are  
 828 evaluated and a dataset of daily PM<sub>2.5</sub> concentration based on aerosol optical depth is used to  
 829 compare and evaluate the estimated PM<sub>2.5</sub> concentration. We analyze the uncertainty and discuss  
 830 the limitations of our dataset. Finally, the PM<sub>2.5</sub> concentration variation (annual calendar cycle,  
 831 interannual cycle and spatial distribution) in 5 regions over the past 64 years is analyzed based on  
 832 GAMM. We hope our dataset will be useful for studying the atmospheric environment, human  
 833 health, and climate change and provide auxiliary support for assimilation. Several key results of this  
 834 study are described as follows:

835 **The most important variable.** Visibility is the most important variable at 80.7% of the PM<sub>2.5</sub> sites,  
836 as visibility can be considered an indicator of PM<sub>2.5</sub> concentration without fog or precipitation. Other  
837 meteorological variables play a secondary role in the model, especially temperature and dew point  
838 temperature.

839 **Model performance and predictive ability.** The training results show that the slope between the  
840 estimated PM<sub>2.5</sub> concentration and the monitored PM<sub>2.5</sub> concentration within the 95% confidence  
841 interval is 0.955, the R<sup>2</sup> is 0.95, the RMSE is 7.2 µg/m<sup>3</sup>, and the MAE is 3.2 µg/m<sup>3</sup>. The test results  
842 show that the slope between the predicted PM<sub>2.5</sub> concentration and the monitored PM<sub>2.5</sub>  
843 concentration is 0.864 ± 0.0010 within a 95% confidence interval, R<sup>2</sup> is 0.79, RMSE is 14.8 µg/m<sup>3</sup>,  
844 and MAE is 7.6 µg/m<sup>3</sup>. The model shows good stability and predictive ability. Compared with a  
845 global PM<sub>2.5</sub> concentration dataset based on satellite retrieval, the slopes of linear regression on the  
846 daily (monthly) scale are 0.817 (0.854) from 2000 to 2021, 0.758 (0.821) from 2000 to 2010, and  
847 0.867 (0.879) from 2011 to 2022. The result indicates the accuracy of the model and the consistency  
848 of the estimated PM<sub>2.5</sub> concentration on the temporal scale.

849 **Regional trends and spatial patterns.** The interannual trends and spatial patterns of PM<sub>2.5</sub>  
850 concentration on the regional scale from 1959 to 2022 are analyzed based on GAMM. In Canada,  
851 the trend is -0.10 µg/m<sup>3</sup>/decade in Canada and the PM<sub>2.5</sub> concentration exhibits an east-high to west-  
852 low pattern. In the United States, the trend is -0.40 µg/m<sup>3</sup>/decade, and PM<sub>2.5</sub> concentration decreases  
853 significantly after 1992, with a trend of -1.39 µg/m<sup>3</sup>/decade. The high PM<sub>2.5</sub> concentration areas are  
854 in the east and west and the low are in the central and northern regions. In Europe, the trend is -1.55  
855 µg/m<sup>3</sup>/decade. High concentration areas are distributed in eastern Europe, while the low is in  
856 northern and western Europe. In China, the trend is 2.09 µg/m<sup>3</sup>/decade. High concentration areas  
857 are distributed in northern China and the low are distributed in southern China and Northern  
858 Tianshan Mountains. The trend is 2.65µg/m<sup>3</sup>/decade from 1959 to 2011 and -22.23 µg/m<sup>3</sup>/decade  
859 from 2012 to 2022. In India, the trend is 0.92 µg/m<sup>3</sup>/decade. The concentration exhibits a north-high  
860 to south-low pattern, with high concentration areas distributed in northern India, such as Ganges  
861 Plain and Thar Desert and the low in Deccan Plateau. The trend is 1.41 µg/m<sup>3</sup>/decade from 1959 to  
862 2013 and -23.36 µg/m<sup>3</sup>/decade from 2014 to 2012. The variation of PM<sub>2.5</sub> concentration is  
863 inseparable with the implementation of pollution control laws and regulations, the energy structure,  
864 industrialization, population and vegetation coverage.

## 865 **7 Data Availability**

866 Daily PM<sub>2.5</sub> concentration data in the Northern Hemisphere from 1959 to 2022 are available at  
867 <https://cstr.cn/18406.11.Atmos.tpc.301127> (Hao et al., 2024).

868 All site-scale PM<sub>2.5</sub> data files are in "PM25-Daily\_1959\_2022.zip". The file name includes a region  
869 name and a site number. For example, the file name, 'China\_1001.txt', means that the site is in  
870 China, and the site number is 1001, which describes the daily PM<sub>2.5</sub> concentration at a single site  
871 and can be directly opened using a text program (such as Notepad), separated by commas. The data  
872 includes four variables: Date, PM25(µg/m<sup>3</sup>), Longitude(degree\_east), and Latitude(degree\_north).  
873 Date is UTC time, PM25(µg/m<sup>3</sup>) is the daily PM<sub>2.5</sub> concentration (unit: µg/m<sup>3</sup>), Longitude range is  
874 [-180 °E, 180 °E] and Latitude range is [0 °N, 90 °N].

## 875 **Competing Interests**

876 The contact author has declared that none of the authors has any competing interests.

## 877 **Acknowledgments**

878 This work was supported by the National Key Research & Development Program of China  
879 (2022YFF0801302) and the National Natural Science Foundation of China (41930970). The hourly  
880 visibility data are available at from [https://www.ncei.noaa.gov/products/land-based-](https://www.ncei.noaa.gov/products/land-based-station/integrated-surface-database)  
881 [station/integrated-surface-database](https://www.ncei.noaa.gov/products/land-based-station/integrated-surface-database). The hourly PM<sub>2.5</sub> data for the United States are available at  
882 <https://www.epa.gov/aqs>. The hourly PM<sub>2.5</sub> data for Canada are available at <https://www.canada.ca>.  
883 The hourly PM<sub>2.5</sub> data for Europe available at <https://european-union.europa.eu>. The hourly PM<sub>2.5</sub>  
884 data for China are available at <https://www.cnemc.cn>. The hourly PM<sub>2.5</sub> data for India are available  
885 at <https://app.cpcbcr.com>. The hourly PM<sub>2.5</sub> concentration data of other regions are from openAQ,  
886 available at <https://openaq.org>. The daily PM<sub>2.5</sub> concentration of long-term gap-free high-resolution  
887 air pollutants (LGHAP) concentration dataset over global land, with a 1 km grid resolution, is  
888 available at [https://zenodo.org/communities/ecnu\\_lghap](https://zenodo.org/communities/ecnu_lghap).

## 889 **References**

- 890 Albrecht, B. A.: Aerosols, cloud microphysics, and fractional cloudiness, *Science*, 245, 1227-1230,  
891 <https://doi.org/10.1126/science.245.4923.1227>, 1989.
- 892 Ali, M. A., Bilal, M., Wang, Y., Nichol, J. E., Mhawish, A., Qiu, Z., de Leeuw, G., Zhang, Y., Zhan, Y.,  
893 Liao, K., Almazroui, M., Dambul, R., Shahid, S., and Islam, M. N.: Accuracy assessment of CAMS and  
894 MERRA-2 reanalysis PM<sub>2.5</sub> and PM<sub>10</sub> concentrations over China, *Atmos. Environ.*, 288, 119297,  
895 <https://doi.org/10.1016/j.atmosenv.2022.119297>, 2022.
- 896 Bai, K., Li, K., Shao, L., Li, X., Liu, C., Li, Z., Ma, M., Han, D., Sun, Y., Zheng, Z., Li, R., Chang, N.  
897 B., and Guo, J.: LGHAP v2: a global gap-free aerosol optical depth and PM<sub>2.5</sub> concentration dataset  
898 since 2000 derived via big Earth data analytics, *Earth Syst. Sci. Data*, 16, 2425-2448,  
899 <https://doi.org/10.5194/essd-16-2425-2024>, 2024.
- 900 Beckerman, B. S., Jerrett, M., Serre, M., Martin, R. V., Lee, S.-J., Van Donkelaar, A., Ross, Z., Su, J.,  
901 and Burnett, R. T.: A hybrid approach to estimating national scale spatiotemporal variability of PM<sub>2.5</sub>  
902 in the contiguous United States, *Environ. Sci. Technol.*, 47, 7233-7241,  
903 <https://doi.org/10.1021/es400039u>, 2013.
- 904 Bergstrom, R. W., Pilewskie, P., Russell, P. B., Redemann, J., Bond, T. C., Quinn, P. K., and Sierau, B.:  
905 Spectral absorption properties of atmospheric aerosols, *Atmos. Chem. Phys.*, 7, 5937-5943,  
906 <https://doi.org/10.5194/acp-7-5937-2007>, 2007.
- 907 Boers, R., van Weele, M., van Meijgaard, E., Savenije, M., Siebesma, A. P., Bosveld, F., and Stammes,  
908 P.: Observations and projections of visibility and aerosol optical thickness (1956-2100) in the  
909 Netherlands: impacts of time-varying aerosol composition and hygroscopicity, *Environ. Res. Lett.*, 10,  
910 <https://doi.org/10.1088/1748-9326/10/1/015003>, 2015.
- 911 Boys, B., Martin, R., Van Donkelaar, A., MacDonell, R., Hsu, N., Cooper, M., Yantosca, R., Lu, Z.,  
912 Streets, D., and Zhang, Q.: Fifteen-year global time series of satellite-derived fine particulate matter,  
913 *Environ. Sci. Technol.*, 48, 11109-11118, <https://doi.org/10.1021/es502113p>, 2014.
- 914 Browne, M. W.: Cross-validation methods, *J. Math. Psychol.*, 44, 108-132,  
915 <https://doi.org/10.1006/jmps.1999.1279>, 2000.



916 Buchard, V., da Silva, A. M., Colarco, P. R., Darmenov, A., Randles, C. A., Govindaraju, R., Torres, O.,  
917 Campbell, J., and Spurr, R.: Using the OMI aerosol index and absorption aerosol optical depth to evaluate  
918 the NASA MERRA Aerosol Reanalysis, *Atmos. Chem. Phys.*, 15, 5743-5760,  
919 <https://doi.org/10.5194/acp-15-5743-2015>, 2015.

920 Buchard, V., da Silva, A. M., Randles, C. A., Colarco, P., Ferrare, R., Hair, J., Hostetler, C., Tackett, J.,  
921 and Winker, D.: Evaluation of the surface PM<sub>2.5</sub> in Version 1 of the NASA MERRA Aerosol Reanalysis  
922 over the United States, *Atmos. Environ.*, 125, 100-111, <https://doi.org/10.1016/j.atmosenv.2015.11.004>,  
923 2016.

924 Buchard, V., Randles, C. A., da Silva, A. M., Darmenov, A., Colarco, P. R., Govindaraju, R., Ferrare, R.,  
925 Hair, J., Beyersdorf, A. J., Ziemba, L. D., and Yu, H.: The MERRA-2 Aerosol Reanalysis, 1980 Onward.  
926 Part II: Evaluation and Case Studies, *J. Climate*, 30, 6851-6872, [https://doi.org/10.1175/JCLI-D-16-](https://doi.org/10.1175/JCLI-D-16-0613.1)  
927 [0613.1](https://doi.org/10.1175/JCLI-D-16-0613.1), 2017.

928 Chafe, Z. A., Brauer, M., Klimont, Z., Van Dingenen, R., Mehta, S., Rao, S., Riahi, K., Dentener, F., and  
929 Smith, K. R.: Household Cooking with Solid Fuels Contributes to Ambient PM<sub>2.5</sub> Air Pollution and the  
930 Burden of Disease, *Environ. Health Persp.*, 122, 1314-1320, <https://doi.org/10.1289/ehp.1206340>, 2014.

931 Chang, K.-L., Petropavlovskikh, I., Cooper, O. R., Schultz, M. G., and Wang, T.: Regional trend analysis  
932 of surface ozone observations from monitoring networks in eastern North America, Europe and East Asia,  
933 *Elementa: Science of the Anthropocene*, 5, <https://doi.org/10.1525/elementa.243>, 2017.

934 Che, H., Xia, X., Zhu, J., Hong, W., and Shi, G.: Aerosol optical properties under the condition of heavy  
935 haze over an urban site of Beijing, China, *Environ. Sci. Pollut. R.*, 22, 1043-1053,  
936 <https://doi.org/10.1007/s11356-014-3415-5>, 2014.

937 Chen, A., Zhao, C., and Fan, T.: Spatio-temporal distribution of aerosol direct radiative forcing over mid-  
938 latitude regions in north hemisphere estimated from satellite observations, *Atmos. Res.*, 266, 105938,  
939 <https://doi.org/10.1016/j.atmosres.2021.105938>, 2022.

940 Chen, Z., Chen, D., Zhao, C., Kwan, M.-p., Cai, J., Zhuang, Y., Zhao, B., Wang, X., Chen, B., Yang, J.,  
941 Li, R., He, B., Gao, B., Wang, K., and Xu, B.: Influence of meteorological conditions on  
942 PM<sub>2.5</sub> concentrations across China: A review of methodology and mechanism, *Environ.*  
943 *Int.*, 139, <https://doi.org/10.1016/j.envint.2020.105558>, 2020.

944 Chow, J. C., Doraiswamy, P., Watson, J. G., Chen, L. W. A., Ho, S. S. H., and Sodeman, D. A.: Advances  
945 in Integrated and Continuous Measurements for Particle Mass and Chemical Composition, *Japca J. Air*  
946 *Waste Ma.*, 58, 141-163, <https://doi.org/10.3155/1047-3289.58.2.141>, 2008.

947 Cohen, A. J., Brauer, M., Burnett, R., Anderson, H. R., Frostad, J., Estep, K., Balakrishnan, K.,  
948 Brunekreef, B., Dandona, L., Dandona, R., Feigin, V., Freedman, G., Hubbell, B., Jobling, A., Kan, H.,  
949 Knibbs, L., Liu, Y., Martin, R., Morawska, L., Pope, C. A., III, Shin, H., Straif, K., Shaddick, G., Thomas,  
950 M., van Dingenen, R., van Donkelaar, A., Vos, T., Murray, C. J. L., and Forouzanfar, M. H.: Estimates  
951 and 25-year trends of the global burden of disease attributable to ambient air pollution: an analysis of  
952 data from the Global Burden of Diseases Study 2015, *Lancet*, 389, 1907-1918,  
953 [https://doi.org/10.1016/s0140-6736\(17\)30505-6](https://doi.org/10.1016/s0140-6736(17)30505-6), 2017.

954 Dabek-Zlotorzynska, E., Dann, T. F., Martinelango, P. K., Celo, V., Brook, J. R., Mathieu, D., Ding, L.,  
955 and Austin, C. C.: Canadian National Air Pollution Surveillance (NAPS) PM<sub>2.5</sub> speciation  
956 program: Methodology and PM<sub>2.5</sub> chemical composition for the years 2003-2008, *Atmos.*  
957 *Environ.*, 45, 673-686, <https://doi.org/10.1016/j.atmosenv.2010.10.024>, 2011.

958 Davies, J.: CEPA—The Canadian Environmental Protection Act, *JAPCA*, 38, 1111-1113,  
959 <https://doi.org/10.1080/08940630.1988.10466452>, 1988.



960 Demerjian, K. L.: A review of national monitoring networks in North America, *Atmos. Environ.*, 34,  
961 1861-1884, [https://doi.org/10.1016/S1352-2310\(99\)00452-5](https://doi.org/10.1016/S1352-2310(99)00452-5), 2000.

962 Fan, H., Zhao, C., Yang, Y., and Yang, X.: Spatio-Temporal Variations of the  
963 PM<sub>2.5</sub>/PM<sub>10</sub> Ratios and Its Application to Air Pollution Type Classification  
964 in China, *Front. Environ. Sci.*, 9, <https://doi.org/10.3389/fenvs.2021.692440>, 2021.

965 Friedman, J. H.: Greedy function approximation: A gradient boosting machine, *Ann. Stat.*, 29, 1189-1232,  
966 <https://doi.org/10.1214/aos/1013203451>, 2001.

967 Ganguly, T., Selvaraj, K. L., and Guttikunda, S. K.: National Clean Air Programme (NCAP) for Indian  
968 cities: Review and outlook of clean air action plans, *Atmospheric Environment X*, 8, 100096,  
969 <https://doi.org/10.1016/j.aeaoa.2020.100096>, 2020.

970 Gelaro, R., McCarty, W., Suárez, M. J., Todling, R., Molod, A., Takacs, L., Randles, C. A., Darmenov,  
971 A., Bosilovich, M. G., Reichle, R., Wargan, K., Coy, L., Cullather, R., Draper, C., Akella, S., Buchard,  
972 V., Conaty, A., da Silva, A. M., Gu, W., Kim, G.-K., Koster, R., Lucchesi, R., Merkova, D., Nielsen, J.  
973 E., Partyka, G., Pawson, S., Putman, W., Rienecker, M., Schubert, S. D., Sienkiewicz, M., and Zhao, B.:  
974 The Modern-Era Retrospective Analysis for Research and Applications, Version 2 (MERRA-2), *J.*  
975 *Climate*, 30, 5419-5454, <https://doi.org/10.1175/JCLI-D-16-0758.1>, 2017.

976 Goff, J. A.: Saturation pressure of water on the new Kelvin temperature scale, *Transactions of the*  
977 *American Society of Heating and Ventilating Engineers*, 63, 347-354, 1957.

978 Granier, C., Bessagnet, B., Bond, T., D'Angiola, A., Denier van der Gon, H., Frost, G. J., Heil, A., Kaiser,  
979 J. W., Kinne, S., and Klimont, Z.: Evolution of anthropogenic and biomass burning emissions of air  
980 pollutants at global and regional scales during the 1980–2010 period, *Climatic Change*, 109, 163-190,  
981 <https://doi.org/10.1007/s10584-011-0154-1>, 2011.

982 Green, D. and Fuller, G. W.: The implications of tapered element oscillating microbalance (TEOM)  
983 software configuration on particulate matter measurements in the UK and Europe, *Atmos. Environ.*, 40,  
984 5608-5616, <https://doi.org/10.1016/j.atmosenv.2006.04.052>, 2006.

985 Gui, K., Che, H., Zeng, Z., Wang, Y., Zhai, S., Wang, Z., Luo, M., Zhang, L., Liao, T., and Zhao, H.:  
986 Construction of a virtual PM<sub>2.5</sub> observation network in China based on high-density surface  
987 meteorological observations using the Extreme Gradient Boosting model, *Environ. Int.*, 141, 105801,  
988 <https://doi.org/10.1016/j.envint.2020.105801>, 2020.

989 Guo, S., Hu, M., Zamora, M. L., Peng, J., Shang, D., Zheng, J., Du, Z., Wu, Z., Shao, M., Zeng, L.,  
990 Molina, M. J., and Zhang, R.: Elucidating severe urban haze formation in China, *P. Natl. A. Sci.*, 111,  
991 17373-17378, <https://doi.org/10.1073/pnas.1419604111>, 2014.

992 Hall, E. and Gilliam, J.: Reference and Equivalent Methods Used to Measure National Ambient Air  
993 Quality Standards (NAAQS) Criteria Air Pollutants - Volume I,  
994 <https://doi.org/10.13140/RG.2.1.3471.8329>, 2016.

995 Hammer, M. S., van Donkelaar, A., Li, C., Lyapustin, A., Sayer, A. M., Hsu, N. C., Levy, R. C., Garay,  
996 M. J., Kalashnikova, O. V., and Kahn, R. A.: Global estimates and long-term trends of fine particulate  
997 matter concentrations (1998–2018), *Environ. Sci. Technol.*, 54, 7879-7890,  
998 <https://doi.org/10.1021/acs.est.0c01764>, 2020.

999 Hao, H., Wang, K., Wu, G., Liu, J., and Li, J.: PM<sub>2.5</sub> concentrations based on near-surface visibility at  
1000 4011 sites in the Northern Hemisphere from 1959 to 2022, National Tibetan Plateau Data Center [dataset],  
1001 <https://doi.org/10.11888/Atmos.tpdc.301127>, 2024.

1002 Hastie, T. and Tibshirani, R.: Generalized Additive Models: Some Applications, *J. Am. Stat. Assoc.*, 82,  
1003 371-386, <https://doi.org/10.1080/01621459.1987.10478440>, 1987.

1004 He, Q., Gao, K., Zhang, L., Song, Y., and Zhang, M.: Satellite-derived 1-km estimates and long-term  
1005 trends of PM<sub>2.5</sub> concentrations in China from 2000 to 2018, *Environ. Int.*, 156, 106726,  
1006 <https://doi.org/10.1016/j.envint.2021.106726>, 2021.

1007 Hsu, N., Lee, J., Sayer, A., Carletta, N., Chen, S. H., Tucker, C., Holben, B., and Tsay, S. C.: Retrieving  
1008 near-global aerosol loading over land and ocean from AVHRR, *J. Geophys. Res-Atmos.*, 122, 9968-  
1009 9989, <https://doi.org/10.1002/2017JD026932>, 2017.

1010 Huang, W., Tan, J., Kan, H., Zhao, N., Song, W., Song, G., Chen, G., Jiang, L., Jiang, C., and Chen, R.:  
1011 Visibility, air quality and daily mortality in Shanghai, China, *Sci. Total Environ.*, 407, 3295-3300,  
1012 <https://doi.org/10.1016/j.scitotenv.2009.02.019>, 2009.

1013 Husar, R. B., Husar, J. D., and Martin, L.: Distribution of continental surface aerosol extinction based on  
1014 visual range data, *Atmos. Environ.*, 34, 5067-5078, [https://doi.org/10.1016/s1352-2310\(00\)00324-1](https://doi.org/10.1016/s1352-2310(00)00324-1),  
1015 2000.

1016 Inness, A., Ades, M., Agustí-Panareda, A., Barré, J., Benedictow, A., Blechschmidt, A.-M., Dominguez,  
1017 J. J., Engelen, R., Eskes, H., and Flemming, J.: The CAMS reanalysis of atmospheric composition, *Atmos.*  
1018 *Chem. Phys.*, 19, 3515-3556, <https://doi.org/10.5194/acp-19-3515-2019>, 2019.

1019 Jin, C., Wang, Y., Li, T., and Yuan, Q.: Global validation and hybrid calibration of CAMS and MERRA-  
1020 2 PM<sub>2.5</sub> reanalysis products based on OpenAQ platform, *Atmos. Environ.*, 274, 118972,  
1021 <https://doi.org/10.1016/j.atmosenv.2022.118972>, 2022.

1022 Kammann, E. E. and Wand, M. P.: Geoadditive Models, *J. R. Stat. Soc. C-appl.*, 52, 1-18,  
1023 <https://doi.org/10.1111/1467-9876.00385>, 2003.

1024 Kendall, M. G.: Rank correlation methods, 1948.

1025 Kim, K.-H., Kabir, E., and Kabir, S.: A review on the human health impact of airborne particulate matter,  
1026 *Environ. Int.*, 74, 136-143, <https://doi.org/10.1016/j.envint.2014.10.005>, 2015.

1027 Kuklinska, K., Wolska, L., and Namiesnik, J.: Air quality policy in the US and the EU—a review, *Atmos.*  
1028 *Pollut. Res.*, 6, 129-137, <https://doi.org/10.5094/APR.2015.015>, 2015.

1029 Lelieveld, J., Evans, J. S., Fnais, M., Giannadaki, D., and Pozzer, A.: The contribution of outdoor air  
1030 pollution sources to premature mortality on a global scale, *Nature*, 525, 367-+,  
1031 <https://doi.org/10.1038/nature15371>, 2015.

1032 Li, C., Martin, R. V., Boys, B. L., van Donkelaar, A., and Ruzzante, S.: Evaluation and application of  
1033 multi-decadal visibility data for trend analysis of atmospheric haze, *Atmos. Chem. Phys.*, 16, 2435-2457,  
1034 <https://doi.org/10.5194/acp-16-2435-2016>, 2016.

1035 Li, C., Martin, R. V., van Donkelaar, A., Boys, B. L., Hammer, M. S., Xu, J.-W., Marais, E. A., Reff, A.,  
1036 Strum, M., and Ridley, D. A.: Trends in chemical composition of global and regional population-  
1037 weighted fine particulate matter estimated for 25 years, *Environ. Sci. Technol.*, 51, 11185-11195,  
1038 <https://doi.org/10.1021/acs.est.7b02530>, 2017.

1039 Li, J., Han, X., Jin, M., Zhang, X., and Wang, S.: Globally analysing spatiotemporal trends of  
1040 anthropogenic PM<sub>2.5</sub> concentration and population's PM<sub>2.5</sub> exposure from 1998 to 2016, *Environ. Int.*,  
1041 128, 46-62, <https://doi.org/10.1016/j.envint.2019.04.026>, 2019.

1042 Li, J., Garshick, E., Hart, J. E., Li, L., Shi, L., Al-Hemoud, A., Huang, S., and Koutrakis, P.: Estimation  
1043 of ambient PM<sub>2.5</sub> in Iraq and Kuwait from 2001 to 2018 using machine learning and remote sensing,  
1044 *Environ. Int.*, 151, <https://doi.org/10.1016/j.envint.2021.106445>, 2021.

1045 Li, J., Carlson, B. E., Yung, Y. L., Lv, D., Hansen, J., Penner, J. E., Liao, H., Ramaswamy, V., Kahn, R.  
1046 A., Zhang, P., Dubovik, O., Ding, A., Laci, A. A., Zhang, L., and Dong, Y.: Scattering and absorbing  
1047 aerosols in the climate system, *Nat. Rev. Earth. Environ.*, 3, 363-379, <https://doi.org/10.1038/s43017->

1048 [022-00296-7](https://doi.org/10.1016/j.atmosenv.2022.022-00296-7), 2022.

1049 Li, S., Chen, L., Huang, G., Lin, J., Yan, Y., Ni, R., Huo, Y., Wang, J., Liu, M., and Weng, H.: Retrieval  
1050 of surface PM<sub>2.5</sub> mass concentrations over North China using visibility measurements and GEOS-Chem  
1051 simulations, *Atmos. Environ.*, 222, 117121, <https://doi.org/10.1016/j.atmosenv.2019.117121>, 2020.

1052 Liao, H., Chang, W., and Yang, Y.: Climatic Effects of Air Pollutants over China: A Review, *Adv. Atmos.*  
1053 *Sci.*, 32, 115-139, <https://doi.org/10.1007/s00376-014-0013-x>, 2015.

1054 Lim, C.-H., Ryu, J., Choi, Y., Jeon, S. W., and Lee, W.-K.: Understanding global PM<sub>2.5</sub> concentrations  
1055 and their drivers in recent decades (1998–2016), *Environ. Int.*, 144, 106011,  
1056 <https://doi.org/10.1016/j.envint.2020.106011>, 2020.

1057 Liu, M., Bi, J., and Ma, Z.: Visibility-based PM<sub>2.5</sub> concentrations in China: 1957–1964 and 1973–2014,  
1058 *Environ. Sci. Technol.*, 51, 13161-13169, <https://doi.org/10.1021/acs.est.7b03468>, 2017.

1059 Liu, M., Huang, X., Song, Y., Tang, J., Cao, J., Zhang, X., Zhang, Q., Wang, S., Xu, T., Kang, L., Cai,  
1060 X., Zhang, H., Yang, F., Wang, H., Yu, J. Z., Lau, A. K. H., He, L., Huang, X., Duan, L., Ding, A., Xue,  
1061 L., Gao, J., Liu, B., and Zhu, T.: Ammonia emission control in China would mitigate haze pollution and  
1062 nitrogen deposition, but worsen acid rain, *P. Natl. A. Sci.*, 116, 7760-7765,  
1063 <https://doi.org/10.1073/pnas.1814880116>, 2019.

1064 Ma, Z., Hu, X., Sayer, A. M., Levy, R., Zhang, Q., Xue, Y., Tong, S., Bi, J., Huang, L., and Liu, Y.:  
1065 Satellite-based spatiotemporal trends in PM<sub>2.5</sub> concentrations: China, 2004–2013, *Environ. Health*  
1066 *Persp.*, 124, 184-192, <https://doi.org/10.1289/ehp.1409481>, 2016.

1067 Mandal, S., Madhipatla, K. K., Guttikunda, S., Kloog, I., Prabhakaran, D., Schwartz, J. D., and Team, G.  
1068 H. I.: Ensemble averaging based assessment of spatiotemporal variations in ambient PM<sub>2.5</sub>  
1069 concentrations over Delhi, India, during 2010–2016, *Atmos. Environ.*, 224, 117309,  
1070 <https://doi.org/10.1016/j.atmosenv.2020.117309>, 2020.

1071 Mann, H. B.: Nonparametric Tests Against Trend, *Econometrica*, 13, 245-259,  
1072 <https://doi.org/10.2307/1907187>, 1945.

1073 Meng, X., Hand, J. L., Schichtel, B. A., and Liu, Y.: Space-time trends of PM<sub>2.5</sub> constituents in the  
1074 conterminous United States estimated by a machine learning approach, 2005–2015, *Environ. Int.*, 121,  
1075 1137-1147, <https://doi.org/10.1016/j.envint.2018.10.029>, 2018.

1076 Miao, Y. and Liu, S.: Linkages between aerosol pollution and planetary boundary layer structure in China,  
1077 *Sci. Total Environ.*, 650, 288-296, <https://doi.org/10.1016/j.scitotenv.2018.09.032>, 2019.

1078 Molnár, A., Mészáros, E., Imre, K., and Rüll, A.: Trends in visibility over Hungary between 1996 and  
1079 2002, *Atmos. Environ.*, 42, 2621-2629, <https://doi.org/10.1016/j.atmosenv.2007.05.012>, 2008.

1080 Nagaraja Rao, C., Stowe, L., and McClain, E.: Remote sensing of aerosols over the oceans using AVHRR  
1081 data Theory, practice and applications, *Int. J. Remote Sens.*, 10, 743-749,  
1082 <https://doi.org/10.1080/01431168908903915>, 1989.

1083 NOAA, DOD, FAA, and USN: Automated Surface Observing System (ASOS) User's Guide, 1998.

1084 Pant, P., Lal, R. M., Guttikunda, S. K., Russell, A. G., Nagpure, A. S., Ramaswami, A., and Peltier, R. E.:  
1085 Monitoring particulate matter in India: recent trends and future outlook, *Air. Qual. Tmos. Hlth.*, 12, 45-  
1086 58, <https://doi.org/10.1007/s11869-018-0629-6>, 2019.

1087 Park, A., Guillas, S., and Petropavlovskikh, I.: Trends in stratospheric ozone profiles using functional  
1088 mixed models, *Atmos. Chem. Phys.*, 13, 11473-11501, <https://doi.org/10.5194/acp-13-11473-2013>, 2013.

1089 Polansky, L. and Robbins, M. M.: Generalized additive mixed models for disentangling long-term trends,  
1090 local anomalies, and seasonality in fruit tree phenology, *Ecol. Evol.*, 3, 3141-3151,  
1091 <https://doi.org/10.1002/ece3.707>, 2013.

1092 Pui, D. Y. H., Chen, S.-C., and Zuo, Z.: PM<sub>2.5</sub> in China: Measurements, sources, visibility and health  
1093 effects, and mitigation, *Particuology*, 13, 1-26, <https://doi.org/10.1016/j.partic.2013.11.001>, 2014.

1094 Qi, G., Wei, W., Wang, Z., Wang, Z., and Wei, L.: The spatial-temporal evolution mechanism of PM<sub>2.5</sub>  
1095 concentration based on China's climate zoning, *J. Environ. Manage.*, 325, 116671,  
1096 <https://doi.org/10.1016/j.jenvman.2022.116671>, 2023.

1097 Ramanathan, V., Crutzen, P. J., Kiehl, J., and Rosenfeld, D.: Aerosols, climate, and the hydrological cycle,  
1098 *Science*, 294, 2119-2124, <https://doi.org/10.1126/science.1064034>, 2001.

1099 Ravindra, K., Rattan, P., Mor, S., and Aggarwal, A. N.: Generalized additive models: Building evidence  
1100 of air pollution, climate change and human health, *Environ. Int.*, 132, 104987,  
1101 <https://doi.org/10.1016/j.envint.2019.104987>, 2019.

1102 Ravindra, K., Vakacherla, S., Singh, T., Upadhy, A. R., Rattan, P., and Mor, S.: Long-term trend of  
1103 PM<sub>2.5</sub> over five Indian megacities using a new statistical approach, *Stoch. Env. Res. Risk A.*, 38, 715-  
1104 725, <https://doi.org/10.1007/s00477-023-02595-x>, 2024.

1105 Samset, B. H., Lund, M. T., Bollasina, M., Myhre, G., and Wilcox, L.: Emerging Asian aerosol patterns,  
1106 *Nat. Geosci.*, 12, 582-584, <https://doi.org/10.1038/s41561-019-0424-5>, 2019.

1107 Sen, P. K.: Estimates of the Regression Coefficient Based on Kendall's Tau, *J. Am. Stat. Assoc.*, 63, 1379-  
1108 1389, <https://doi.org/10.1080/01621459.1968.10480934>, 1968.

1109 Shen, Z., Cao, J., Zhang, L., Zhang, Q., Huang, R.-J., Liu, S., Zhao, Z., Zhu, C., Lei, Y., and Xu, H.:  
1110 Retrieving historical ambient PM<sub>2.5</sub> concentrations using existing visibility measurements in Xi'an,  
1111 Northwest China, *Atmos. Environ.*, 126, 15-20, <https://doi.org/10.1016/j.atmosenv.2015.11.040>, 2016.

1112 Shi, Y., Matsunaga, T., Yamaguchi, Y., Li, Z., Gu, X., and Chen, X.: Long-term trends and spatial patterns  
1113 of satellite-retrieved PM<sub>2.5</sub> concentrations in South and Southeast Asia from 1999 to 2014, *Sci. Total*  
1114 *Environ.*, 615, 177-186, <https://doi.org/10.1016/j.scitotenv.2017.09.241>, 2018.

1115 Singh, A., Avis, W. R., and Pope, F. D.: Visibility as a proxy for air quality in East Africa, *Environ. Res.*  
1116 *Lett.*, 15, 084002, <https://doi.org/10.1088/1748-9326/ab8b12>, 2020.

1117 Singh, V., Singh, S., and Biswal, A.: Exceedances and trends of particulate matter (PM<sub>2.5</sub>) in five Indian  
1118 megacities, *Sci. Total Environ.*, 750, 141461, <https://doi.org/10.1016/j.scitotenv.2020.141461>, 2021.

1119 Smith, A., Lott, N., and Vose, R.: The Integrated Surface Database: Recent Developments and  
1120 Partnerships, *B. Am. Meteorol. Soc.*, 92, 704-708, <https://doi.org/10.1175/2011BAMS3015.1>, 2011.

1121 Su, L., Gao, C., Ren, X., Zhang, F., Cao, S., Zhang, S., Chen, T., Liu, M., Ni, B., and Liu, M.:  
1122 Understanding the spatial representativeness of air quality monitoring network and its application to  
1123 PM<sub>2.5</sub> in the mainland China, *Geosci. Front.*, 13, 101370, <https://doi.org/10.1016/j.gsf.2022.101370>,  
1124 2022.

1125 Sun, E., Xu, X., Che, H., Tang, Z., Gui, K., An, L., Lu, C., and Shi, G.: Variation in MERRA-2 aerosol  
1126 optical depth and absorption aerosol optical depth over China from 1980 to 2017, *J. Atmos. Sol-Terr.*  
1127 *Phy.*, 186, 8-19, <https://doi.org/10.1016/j.jastp.2019.01.019>, 2019.

1128 Tan, S., Wang, Y., Yuan, Q., Zheng, L., Li, T., Shen, H., and Zhang, L.: Reconstructing global PM<sub>2.5</sub>  
1129 monitoring dataset from OpenAQ using a two-step spatio-temporal model based on SES-IDW and LSTM,  
1130 *Environ. Res. Lett.*, 17, 034014, <https://doi.org/10.1088/1748-9326/ac52c9>, 2022.

1131 Theil, H.: A Rank-Invariant Method of Linear and Polynomial Regression Analysis, in: *Henri Theil's*  
1132 *Contributions to Economics and Econometrics: Econometric Theory and Methodology*, edited by: Raj,  
1133 B., and Koerts, J., Springer Netherlands, Dordrecht, 345-381, [https://doi.org/10.1007/978-94-011-2546-  
1134 8\\_20](https://doi.org/10.1007/978-94-011-2546-8_20), 1992.

1135 Van Donkelaar, A., Martin, R. V., and Park, R. J.: Estimating ground-level PM<sub>2.5</sub> using aerosol optical

1136 depth determined from satellite remote sensing, *J. Geophys. Res.*, 111,  
1137 <https://doi.org/10.1029/2005JD006996>, 2006.

1138 Van Donkelaar, A., Martin, R. V., Brauer, M., and Boys, B. L.: Use of satellite observations for long-term  
1139 exposure assessment of global concentrations of fine particulate matter, *Environ. Health Persp.*, 123,  
1140 135-143, <https://doi.org/10.1289/ehp.1408646>, 2015.

1141 Van Donkelaar, A., Martin, R. V., Brauer, M., Kahn, R., Levy, R., Verduzco, C., and Villeneuve, P. J.:  
1142 Global estimates of ambient fine particulate matter concentrations from satellite-based aerosol optical  
1143 depth: development and application, *Environ. Health Persp.*, 118, 847-855,  
1144 <https://doi.org/10.1289/ehp.0901623>, 2010.

1145 Van Donkelaar, A., Martin, R. V., Brauer, M., Hsu, N. C., Kahn, R. A., Levy, R. C., Lyapustin, A., Sayer,  
1146 A. M., and Winker, D. M.: Global estimates of fine particulate matter using a combined geophysical-  
1147 statistical method with information from satellites, models, and monitors, *Environ. Sci. Technol.*, 50,  
1148 3762-3772, <https://doi.org/10.1021/acs.est.5b05833>, 2016.

1149 van Donkelaar, A., Hammer, M. S., Bindle, L., Brauer, M., Brook, J. R., Garay, M. J., Hsu, N. C.,  
1150 Kalashnikova, O. V., Kahn, R. A., Lee, C., Levy, R. C., Lyapustin, A., Sayer, A. M., and Martin, R. V.:  
1151 Monthly Global Estimates of Fine Particulate Matter and Their Uncertainty, *Environ. Sci. Technol.*, 55,  
1152 15287-15300, <https://doi.org/10.1021/acs.est.1c05309>, 2021.

1153 Verbeke, G. and Lesaffre, E.: A Linear Mixed-Effects Model with Heterogeneity in the Random-Effects  
1154 Population, *J. Am. Stat. Assoc.*, 91, 217-221, <https://doi.org/10.1080/01621459.1996.10476679>, 1996.

1155 Viana, M., Kuhlbusch, T. A. J., Querol, X., Alastuey, A., Harrison, R. M., Hopke, P. K., Winiwarter, W.,  
1156 Vallius, A., Szidat, S., Prevot, A. S. H., Hueglin, C., Bloemen, H., Wahlin, P., Vecchi, R., Miranda, A. I.,  
1157 Kasper-Giebl, A., Maenhaut, W., and Hitzenberger, R.: Source apportionment of particulate matter in  
1158 Europe: A review of methods and results, *J. Aerosol Sci.*, 39, 827-849,  
1159 <https://doi.org/10.1016/j.jaerosci.2008.05.007>, 2008.

1160 Wang, K., Dickinson, R. E., and Liang, S.: Clear Sky Visibility Has Decreased over Land Globally from  
1161 1973 to 2007, *Science*, 323, 1468-1470, <https://doi.org/10.1126/science.1167549>, 2009.

1162 Wang, K. C., Dickinson, R. E., Su, L., and Trenberth, K. E.: Contrasting trends of mass and optical  
1163 properties of aerosols over the Northern Hemisphere from 1992 to 2011, *Atmos. Chem. Phys.*, 12, 9387-  
1164 9398, <https://doi.org/10.5194/acp-12-9387-2012>, 2012.

1165 Wang, Q., Kwan, M.-P., Zhou, K., Fan, J., Wang, Y., and Zhan, D.: The impacts of urbanization on fine  
1166 particulate matter (PM<sub>2.5</sub>) concentrations: Empirical evidence from 135 countries worldwide, *Environ.*  
1167 *Pollut.*, 247, 989-998, <https://doi.org/10.1016/j.envpol.2019.01.086>, 2019.

1168 Wang, Z., Li, J., Wang, Z., Yang, W., Tang, X., Ge, B., Yan, P., Zhu, L., Chen, X., Chen, H., Wand, W.,  
1169 Li, J., Liu, B., Wang, X., Wand, W., Zhao, Y., Lu, N., and Su, D.: Modeling study of regional severe hazes  
1170 over mid-eastern China in January 2013 and its implications on pollution prevention and control, *Sci.*  
1171 *China Earth Sci.*, 57, 3-13, <https://doi.org/10.1007/s11430-013-4793-0>, 2014.

1172 Wei, J., Li, Z., Peng, Y., and Sun, L.: MODIS Collection 6.1 aerosol optical depth products over land and  
1173 ocean: validation and comparison, *Atmos. Environ.*, 201, 428-440,  
1174 <https://doi.org/10.1016/j.atmosenv.2018.12.004>, 2019a.

1175 Wei, J., Huang, W., Li, Z., Xue, W., Peng, Y., Sun, L., and Cribb, M.: Estimating 1-km-resolution PM<sub>2.5</sub>  
1176 concentrations across China using the space-time random forest approach, *Remote Sens. Environ.*, 231,  
1177 <https://doi.org/10.1016/j.rse.2019.111221>, 2019b.

1178 Wei, J., Li, Z., Lyapustin, A., Sun, L., Peng, Y., Xue, W., Su, T., and Cribb, M.: Reconstructing 1-km-  
1179 resolution high-quality PM<sub>2.5</sub> data records from 2000 to 2018 in China: spatiotemporal variations and



1180 policy implications, *Remote Sens. Environ.*, 252, 112136, <https://doi.org/10.1016/j.rse.2020.112136>,  
1181 2021.

1182 Wei, J., Li, Z., Cribb, M., Huang, W., Xue, W., Sun, L., Guo, J., Peng, Y., Li, J., and Lyapustin, A.:  
1183 Improved 1 km resolution PM 2.5 estimates across China using enhanced space–time extremely  
1184 randomized trees, *Atmos. Chem. Phys.*, 20, 3273–3289, <https://doi.org/10.5194/acp-20-3273-2020>, 2020.

1185 Wood, S. N., Pya, N., and Säfken, B.: Smoothing Parameter and Model Selection for General Smooth  
1186 Models, *J. Am. Stat. Assoc.*, 111, 1548–1563, <https://doi.org/10.1080/01621459.2016.1180986>, 2016.

1187 Wu, J., Zheng, H., Zhe, F., Xie, W., and Song, J.: Study on the relationship between urbanization and fine  
1188 particulate matter (PM<sub>2.5</sub>) concentration and its implication in China, *J. Cleaner Prod.*, 182, 872–882,  
1189 <https://doi.org/10.1016/j.jclepro.2018.02.060>, 2018.

1190 Wu, W. and Zhang, Y.: Effects of particulate matter (PM<sub>2.5</sub>) and associated acidity on ecosystem  
1191 functioning: response of leaf litter breakdown, *Environ. Sci. Pollut. R.*, 25, 30720–30727,  
1192 <https://doi.org/10.1007/s11356-018-2922-1>, 2018.

1193 Xue, T., Zheng, Y., Tong, D., Zheng, B., Li, X., Zhu, T., and Zhang, Q.: Spatiotemporal continuous  
1194 estimates of PM<sub>2.5</sub> concentrations in China, 2000–2016: A machine learning method with inputs from  
1195 satellites, chemical transport model, and ground observations, *Environ. Int.*, 123, 345–357,  
1196 <https://doi.org/10.1016/j.envint.2018.11.075>, 2019.

1197 Yang, X., Zhao, C., Yang, Y., Yan, X., and Fan, H.: Statistical aerosol properties associated with fire  
1198 events from 2002 to 2019 and a case analysis in 2019 over Australia, *Atmos. Chem. Phys.*, 21, 3833–  
1199 3853, <https://doi.org/10.5194/acp-21-3833-2021>, 2021.

1200 Zeng, Z., Gui, K., Wang, Z., Luo, M., Geng, H., Ge, E., An, J., Song, X., Ning, G., and Zhai, S.:  
1201 Estimating hourly surface PM<sub>2.5</sub> concentrations across China from high-density meteorological  
1202 observations by machine learning, *Atmos. Res.*, 254, 105516,  
1203 <https://doi.org/10.1016/j.atmosres.2021.105516>, 2021.

1204 Zhang, Q., Zheng, Y., Tong, D., Shao, M., Wang, S., Zhang, Y., Xu, X., Wang, J., He, H., Liu, W., Ding,  
1205 Y., Lei, Y., Li, J., Wang, Z., Zhang, X., Wang, Y., Cheng, J., Liu, Y., Shi, Q., Yan, L., Geng, G., Hong, C.,  
1206 Li, M., Liu, F., Zheng, B., Cao, J., Ding, A., Gao, J., Fu, Q., Huo, J., Liu, B., Liu, Z., Yang, F., He, K.,  
1207 and Hao, J.: Drivers of improved PM<sub>2.5</sub> air quality in China from 2013 to 2017, *P. Natl. A.*  
1208 *Sci.*, 116, 24463–24469, <https://doi.org/10.1073/pnas.1907956116>, 2019.

1209 Zhang, S., Wu, J., Fan, W., Yang, Q., and Zhao, D.: Review of aerosol optical depth retrieval using  
1210 visibility data, *Earth-Sci. Rev.*, 200, 102986, <https://doi.org/10.1016/j.earscirev.2019.102986>, 2020.

1211 Zhang, Z., Wu, W., Wei, J., Song, Y., Yan, X., Zhu, L., and Wang, Q.: Aerosol optical depth retrieval from  
1212 visibility in China during 1973–2014, *Atmos. Environ.*, 171, 38–48,  
1213 <https://doi.org/10.1016/j.atmosenv.2017.09.004>, 2017.

1214 Zhao, B., Su, Y., He, S., Zhong, M., and Cui, G.: Evolution and comparative assessment of ambient air  
1215 quality standards in China, *J. Integr. Environ. Sci.*, 13, 85–102,  
1216 <https://doi.org/10.1080/1943815X.2016.1150301>, 2016a.

1217 Zhao, S., Yu, Y., Yin, D., He, J., Liu, N., Qu, J., and Xiao, J.: Annual and diurnal variations of gaseous  
1218 and particulate pollutants in 31 provincial capital cities based on in situ air quality monitoring data from  
1219 China National Environmental Monitoring Center, *Environ. Int.*, 86, 92–106,  
1220 <https://doi.org/10.1016/j.envint.2015.11.003>, 2016b.

1221 Zhong, J., Zhang, X., Gui, K., Liao, J., Fei, Y., Jiang, L., Guo, L., Liu, L., Che, H., and Wang, Y.:  
1222 Reconstructing 6-hourly PM 2.5 datasets from 1960 to 2020 in China, *Earth Syst. Sci. Data*, 14, 3197–  
1223 3211, <https://doi.org/10.5194/essd-14-3197-2022>, 2022.

1224 Zhong, J., Zhang, X., Gui, K., Wang, Y., Che, H., Shen, X., Zhang, L., Zhang, Y., Sun, J., and Zhang, W.:  
1225 Robust prediction of hourly PM<sub>2.5</sub> from meteorological data using LightGBM, Natl. Sci. Rev., 8,  
1226 nwaa307, <https://doi.org/10.1093/nsr/nwaa307>, 2021.  
1227